Asian Journal of Pharmaceutical Sciences 18 (2023) 100851

Available online at www.sciencedirect.com

ScienceDirect

journal homepage: www.elsevier.com/locate/AJPS

Original Research Paper

Biomimetic biomineralization nanoplatform-mediated differentiation therapy and phototherapy for cancer stem cell inhibition and antitumor immunity activation

*Shan Gao, Meng Liu, Dongzhu Liu, Xinru Kong, Yuelin Fang, Yingying Li, Hang Wu, Jianbo Ji, Xiaoye Yang, Guangxi Zhai**

Department of Pharmaceutics, Key Laboratory of Chemical Biology (Ministry of Education), NMPA Key Laboratory for Technology Research and Evaluation of Drug Products, School of Pharmaceutical Sciences, Cheeloo College of Medicine, Shandong University, Jinan, Shandong, 250012, China

ARTICLE INFO

Article history:
Received 26 June 2023
Revised 24 August 2023
Accepted 11 September 2023
Available online 30 September 2023

Keywords:
Cancer stem cells
Differentiation therapy
Phototherapy
Biomineralization
Immunogenic cell death

ABSTRACT

Growing evidence suggests that the presence of cancer stem cells (CSCs) is a major challenge in current tumor treatments, especially the transition from non-CSCs to differentiation of CSCs for evading conventional therapies and driving metastasis. Here we propose a therapeutic strategy of synergistic differentiation therapy and phototherapy to induce differentiation of CSCs into mature tumor cells by differentiation inducers and synergistic elimination of them and normal cancer cells through phototherapy. In this work, we synthesized a biomimetic nanoplatform loaded with IR-780 and all-trans retinoic acid (ATRA) *via* biomineralization. This method can integrate aluminum ions into small-sized protein carriers to form nanoclusters, which undergo responsive degradation under acidic conditions and facilitate deep tumor penetration. With the help of CSC differentiation induced by ATRA, IR-780 inhibited the self-renewal of CSCs and cancer progression by generating hyperthermia and reactive oxygen species in a synergistic manner. Furthermore, ATRA can boost immunogenic cell death induced by phototherapy, thereby strongly causing a systemic anti-tumor immune response and efficiently eliminating CSCs and tumor cells. Taken together, this dual strategy represents a new paradigm of targeted eradication of CSCs and tumors by inducing CSC differentiation, improving photothermal therapy/photodynamic therapy and enhancing antitumor immunity.

1. Introduction

Cancer stem cells (CSCs) represent highly malignant cell populations within tumors, and their presence has been

* Corresponding author.
E-mail address: professorgxzhai@126.com (G. Zhai).
Peer review under responsibility of Shenyang Pharmaceutical University.

https://doi.org/10.1016/j.ajps.2023.100851

verified to be the culprit for the tumor recurrence and metastasis [1]. However, traditional chemotherapy and radiotherapy not only cannot successfully eliminate CSCs, but also expand the proportion of CSCs and induce CSCs to enter a dormant state [2]. Therefore, developing therapies targeting CSCs provides a promising strategy for combating and eradicating tumors [3]. Differentiation therapy is a new field of tumor therapeutics research. The difference is that it does not kill tumor cells, but induces CSCs to differentiate into the mature stage under the action of differentiation inducers, and restores the normal or near-normal phenotype and function of cells [4]. With the continuous deepening of research, especially the successful application of differentiation therapy in acute leukemia, it has inspired people to apply this therapy to neuroblastoma, gastric cancer, lung cancer, breast cancer, malignant melanocytes, lymphocyte tumors and other solid tumors [5]. Although most of the research are still in the experimental stage, they have also achieved phased results. ATRA, a vitamin A derivative, is the first-line drug for the treatment of acute promyelocytic leukemia, which induces terminal differentiation in acute promyelocytic leukemogenesis *in vitro* and *in vivo* [6]. In solid tumors, retinoic acid can promote differentiation and apoptosis, inhibit proliferation (block G1 phase), invasion and metastasis [7]. *In vitro* experiments confirmed that ATRA could increase concentration of intracellular ROS and inhibit the proliferation and infiltration of CSCs effectively, resulting in reduced stemness of CSCs for improving the sensitivity of CSCs to antitumor drugs [6].

In recent years, phototherapy including photothermal therapy (PTT) and photodynamic therapy (PDT) has received extensive attention in the field of oncology treatment. Compared with conventional cancer treatment mode, phototherapy has many advantages such as non-invasiveness, good targeting, low toxicity and side effects, and simple operation, which has achieved great success in the clinical treatment of superficial tumors [8,9]. As a typical cancer phototheranostic molecule, IR-780 represents excellent photothermal and photodynamic performance under near-infrared (NIR) laser irradiation [10]. In this approach, IR-780 destroys tumor cells and elicits immunogenic death immunogenic cell death (ICD), accompanied by the release of damage-associated molecular patterns. The ICD effect can increase the proportion of cytotoxic T cells (CTL) and helper T cells (Ths) in tumor microenvironment (TME) and boost the immune status of the body to a certain extent, which contributes to producing potent antitumor immune response [11,12]. Moreover, it has been indicated that the heat generated by PTT achieves uniform temperature distribution and deep penetration in CSC niche, which in turn eliminates CSCs. For example, Wang et al. constructed hydroxyethyl starch-folic acid (HES-FA) conjugate encapsulated with DOX precursor and IR-780 as a nanomedicine to improve the tumor mechanical microenvironment through photothermal effect, which promoted drug delivery and thus removed CSCs [13]. Tan et al. proposed bionic apoferritin nanocages as nanocarriers to achieve deep tumor penetration and improve preferential accessibility of CSCs in tumors through combined photothermal-chemotherapy [14]. However, single-modality phototherapy cannot completely destroy tumor tissues and eradicate CSCs, and there is a risk of tumor metastasis and recurrence. Consequently, the combination of phototherapy and differentiation therapy can solve this problem well, achieve complementary advantages and cooperatively enhance the therapeutic effect [15].

Hypoxia, as a typical feature of TME, has been demonstrated to promote CSCs to exhibit a hypo-differentiated state and form malignant clones to facilitate cell survival and self-renewal. Besides, hypoxia regulates stemness transcription factors in CSCs, such as OCT-4, SOX2, and Nanog, thereby evading the surveillance of the immune system and promoting tumor invasion and metastasis [16,17]. Oxygen carriers based on hemoglobin (Hb) have been extensively studied in tumor therapy to address hypoxia because of their superior oxygen-loading capacity [18]. However, free Hb tetramers are easily depolymerized into dimers, which enter the renal tubules through glomerular filtration and then cause renal damage. Moreover, due to the lack of protection of reductase, free Hb is prone to auto-oxidative reaction under the action of oxygen to generate methemoglobin [19]. This process is often accompanied by the production of numerous superoxide anion, which eventually causes oxidative stress damage to the body. Moreover, Hb is not an excellent oxygen donor due to its poor stability and short circulation time, leading to inefficient oxygen delivery to the tumor region [20]. Consequently, Hb often needs a certain modification to become a safe oxygen carrier. Bovine serum albumin (BSA), as the main component of serum proteins, has been extensively applied to drug delivery because of its inherent biocompatibility, good *in vivo* stability, abundant sources, and a variety of easily modified functional groups [21]. Furthermore, albumin nanoparticles can be specifically targeted to different tissues and organs by controlling their particle size [22], revealing that they have various potential superior functions as intelligent drug carriers [23]. Based on this, the construction of hybrid protein-based nanoparticles as oxygen carriers can greatly reduce the potential side effects of Hb, increase its systemic stability and improve tumor oxygenation specificity [24].

The special microenvironment of solid tumors, such as dense extracellular matrix, disordered vascular system and high interstitial fluid pressure, prevents large-scale therapeutic agents from penetrating into tumors, thus impairing their therapeutic effects [25]. Biomineralization has been reported as a common approach to construct versatile and biocompatible nanoplatforms. For example, Zhang et al. reported a high-efficiency nanovaccine through biomineralization, which comprises the ovalbumin and the Mn-based nanoparticle to activate the cGAS-STING pathway [26]. Besides, a cancer cell membrane-modified redox nano-enzyme was constructed by biomineralization for combined immunotherapy and second near-infrared window (NIR-II) PTT [27]. As one of the most extensively investigated biomineralization methods, the biomineralization of aluminum hydroxide is initiated by adsorption of aluminum ions on BSA and Hb through the affinity of carboxyl and amino groups of protein toward metal ions,

and then triggers the aggregation of nanoparticles by adjusting the pH value through sodium hydroxide [28]. Inspired by the biomineralization method, the special microenvironment of tumors is used to realize the responsive dissociation of nanoclusters and then infiltrate into the tumor tissue, which benefits the therapeutic effect [29].

In light of the above considerations, this study utilized the unique acidic properties of the TME to construct a pH-responsive dissociable nanoplatform with the characteristics of laser response, variable size and prolonged circulatory retention. In this study, it was proposed to encapsulate IR-780 through the hydrophobic cavity of BSA to prepare IR@BSA with PTT and PDT effects. The differentiation inducer ATRA binded to Hb through an amide bond to prepare AT@Hb with differentiation regulation function, in which Hb could carry oxygen and alleviate hypoxia in CSC niche. The ultra-small-sized AT@Hb and IR@BSA nanoparticles were then aggregated through biomineralization method to form size-switchable hybrid protein nanoclusters (IR/AT@HPOC). Finally, the M1 macrophage membrane-coated nanoplatform (M1-IR/AT@HPOC) was prepared by direct extrusion method. The biomimetic nanoplatform can not only delay the clearance of the mononuclear phagocyte system (MPS), but also target the tumor site by leveraging the molecular recognition of tumor cells by various proteins on the M1 macrophage membrane [30,31]. Under the acidic conditions of TME, the biomineralized aluminum hydroxide is degraded in response to releasing the ultra-small nano protein drug delivery carriers, which pass through the tumor stroma and achieve high accumulation in tumors [32]. At meantime, ATRA can strengthen the PTT/PDT effect of IR-780 through decreasing the proportion of CSCs, thereby eliciting the ICD in tumors, promoting the maturation of dendritic cells (DCs) and subsequent activation of T lymphocytes, and then producing potent anti-tumor immune responses [33,34]. Our results demonstrated that the prepared M1-IR/AT@HPOC could inhibit the proliferation and metastasis of tumor cells and CSCs, so as to produce a synergistic anti-tumor therapeutic effect.

2. Materials and methods

2.1. Materials

BSA was obtained from Klontech. IR-780 was purchased from Beijing J&K Technology Co., Ltd. (Beijing, China). ATRA, N-hydroxysuccinimide (NHS), 1-Ethyl-3 (3-dimethylaminopropyl) carbodiimide (EDC), tris (4,7-diphenyl-1,10-phenanthroline) ruthenium dichloride complex (Ru(dpp)3Cl2) and 1, 3-diaphenylisobenzofuran (DPBF) were bought from Shanghai Aladdin Bio-Chem Technology Co., Ltd. Fetal bovine serum (FBS), 1% antibiotic-antimycotic cocktail, hydrocortisone basic fibroblast growth factor (bFGF), epidermal growth factor (EGF) and B27 were provided by Giboc, USA. Cell-counting kit-8 (CCK-8) was obtained from APExBIO Technology LLC. 4′,6-diamidino-2-phenylindole (DAPI), 4% paraformaldehyde, reactive oxygen species assay kit, Mito-Tracker Green, Lyso-tracker green, calreticulin rabbit monoclonal antibody, high mobility group protein B1 (HMGB1) antibody, ATP assay Kit and Alexa Fluor 488-labeled goat anti-rabbit lgG ($H + L$) were all bought from Beyotime Biotech Inc, Shanghai, China. Annexin V/PI cell assay kit was provided by Shanghai Yisheng biotechnology Co., Ltd. (Shanghai, China). Mitochondrial membrane potential assay kit, calcein-AM/PI staining kit and crystal violet were purchased from Beijing Solarbio Science & Technology Co., Ltd. (Beijing, China). Granulocyte macrophage colony stimulating factor (GM-CSF) was purchased from PeproTech Inc. The mouse TNF-α, IL-6, IFN-γ ELISA kits and the antibodies used in western blot of iNOS, Nanog, SOX2, OCT4 were provided by Jiangsu Meimian industrial Co., Ltd. (Jiangsu, China). The antibodies used in animal experiments were all from BioLegend, Inc. Hyaluronidase (HAase) and collagenase were obtained from Dalian Meilun Biological Technology Co., Ltd. (Dalian, China). The immunohistochemical staining were provided by Wuhan Servicebio Technology Co., Ltd.

2.2. Synthesis of AT@Hb, IR@BSA and IR/AT@HPOC

To prepare AT@Hb, ATRA (5.0 mg), NHS (2.0 mg) and EDC (3.2 mg) were mixed in DMSO (1.0 ml) under 25 °C for 2 h to activate the carboxyl groups on ATRA, and subsequently added into deionized water (50 ml) containing Hb (100 mg) under magnetic stirring in the dark for 4 h. The suspension was then dialyzed (molecular weight cutoff (MWCO) =10 kDa) with deionized water for 48 h in a dark environment to remove free ATRA [22]. IR-780 used during this experiment was pre-dispersed in DMSO (10 mg/ml). To obtain IR@BSA, the IR-780 sample was added into BSA solution. The mixture was stirred for 1 h in the dark. After that, free IR-780 was removed by low-speed centrifugation and dialysis [35,36].

To synthesize IR/AT@HPOC, 100 mg IR@BSA and AT@Hb (IR-780 quality: ATRA quality = 1:1) were added in 25 ml deionized water and then slowly added 2 ml aluminum chloride (200 mM) to the suspension with stirring. The solution pH value was then adjusted to 8–9 with the configured NaOH aqueous solution (1.0 M) and the embedded aluminum ions grew rapidly, forming aluminum hydroxide *in situ* in order to polymerize the small-sized nanoparticles together. After 4 h, the solution pH was adjusted to about 7 with citric acid. Finally, the excess aluminum chloride was removed by dialysis (MWCO = 10 kDa) [32].

2.3. Separation of M1 macrophage membranes and preparation of M1-IR/AT@HPOC

M1-polarized macrophages were generated by stimulation of Raw 264.7 cells with lipopolysaccharide (LPS) at the concentration of 1 μg/ml for 24 h as previously described [30]. They were then resuspended and incubated overnight in hypotonic lysis buffer (4 °C). The polarized macrophages were sonicated with a cell disruption probe for 20–25 min and the cells were collected and centrifuged (3200 g, 5 min) to remove nuclei and cytoplasm. The supernatant was centrifuged at 4 °C (1×10^6 rpm, 90 min) to collect the macrophage membrane. The purified M1 macrophage membranes were stored in isotonic solution and contained 0.1 mg/ml protein (from 10^7

cells, 1 ml) by BCA protein determination. The M1 macrophage membranes and IR/AT@HPOC were sequentially extruded 20 times through 800 nm, 400 nm, and 200 nm polycarbonate porous membranes using an Avestin mini extruder to harvest M1-IR/AT@HPOC. The prepared M1-IR/AT@HPOC was stored at 4 °C and used as soon as possible.

2.4. *Identification of stemness-related property and therapeutic effects of nano-preparations*

The stemness-related properties of 4T1 cells were analyzed by using Hoechst side population (SP) method. 4T1 cells were digested, and then the single suspended 4T1 cells were co-incubated with Hoechst 33,342 dye with or without verapamil hydrochloride (100 μM) at 37 °C for 90 min. Hoechst 33,342 was then excited at 350 nm by flow cytometry and dual emission channel analysis was performed (Hoechst blue: 405 nm, Hoechst Red: 670 nm). To investigate the reversal effect of ATRA on stemness-related cells, we incubated tumor cells with ATRA and performed the above experimental protocol [37].

For the culture of CSCs, 4T1 cells were inoculated in ultra-low attachment plates and cultured in DMEM/F12 medium supplemented with 5% B27, 0.4% BSA, 20 ng/ml bFGF and 20 ng/ml EGF for 1 week [38]. To examine the impact of ATRA on cell cycle, CSCs were co-incubated with ATRA of different concentrations for 24 h and stained with 100 μl RNase A solution and 400 μl PI staining solution (Solarbio, CA1510). The treated cells were detected by flow cytometry [39].

The stemness of 4T1 cells and mammosphere-derived CSCs was characterized using flow cytometry. Briefly, 4T1 cells and mammosphere derived CSCs were cultured in ATRA medium or nano-preparations for 24 h and then stained with antibodies (FITC–CD44 and PE-CD24). The levels of CD44 and CD24 were measured by flow cytometry [14].

To explore the expression level of SOX2 and OCT-4, 3D tumorspheres were treated with ATRA of different concentrations or different nano-preparations including free IR-780, free IR+AT, IR@BSA, IR/AT@HPOC and M1-IR/AT@HPOC for 24 h. For the laser irradiation groups, cells were irradiated under NIR laser for 3 min (1.5 W/cm^2) after 12 h of culture and the expressions of SOX2 and OCT-4 markers were determined by western blot.

2.5. *In vivo anti-primary tumor therapy*

To establish mice breast cancer models, 4T1 cells (1×10^6 cells/mouse) were inoculated into the left anterior armpit of Balb/c mice subcutaneously. A week later, when the volume of tumors was close to 100 mm^3, the 4T1 tumor-bearing mice were assigned randomly to eight treatment groups and the samples of saline, free AT, AT@Hb, free IR-780, free IR+AT, IR@BSA, IR/AT@HPOC or M1-IR/AT@HPOC (2.5 mg/kg of IR-780 and 2.5 mg/kg of ATRA) were intravenously injected into the mice every 6 d for 3 times ($n = 5$ for each group). Mice in the laser irradiation groups including free IR-780, free IR+AT, IR@BSA, IR/AT@HPOC and M1-IR/AT@HPOC were then exposed to NIR laser for 5 min (1.5 W/cm^2) 12 h after the intravenous injection. Tumor volume and mouse weight were monitored every 2 d. The blood was isolated from mice on Day 14, and serum samples were collected for analysis. Serum levels of IL-2, TNF-α and IFN-γ were analyzed by ELISA kits to assess the systemic immune efficacy induced by the different preparations. For histological analysis, tumor tissues and main organs from mice were collected and sliced for hematoxylin and eosin (H&E) staining. Furthermore, sections of tumor sites were subjected to TUNEL immunofluorescence staining to assess apoptosis of tumor cells according to the standard protocol reported in the literature. Sections of tumor tissue were stained with CD4 and CD8 to evaluate T cell infiltration at the tumor site and stained with Nanog and SOX2 to assess the stemness characteristics of the tumor tissues. Immunofluorescent staining of hypoxia-inducible factor-1α (HIF-1α) was detected to assess tumor hypoxia.

Subsequently, tumors were digested with collagenase and hyaluronidase to obtain single-cell suspensions for confirming the immune response evoked by the different treatment groups. The tumor tissue suspension was stained with PE-CD24/FITC–CD44 to examine the proportion of CSCs. Lymphocytes from the tumor-infiltrating tissues were isolated following the instructions of the Tumor-Infiltrating Lymphocyte Cell Isolation Medium Kit (Mouse). The lymphocytes extracted from tumors were resuspended in PBS and stained with FITC–CD3, APC–CD4 and PE-CD8a. Besides, the spleens and lymph nodes in each group were ground and centrifuged to extract immune cells as previously reported. For analysis of the activation of DCs in lymph nodes, cells were stained with APC–CD11c, PE-CD86 and FITC–CD80. To detect the activation of T lymphocytes, splenocytes were stained for Ths (FITC–CD3 and APC–CD4) and CTLs (FITC–CD3 and PE-CD8a), respectively.

2.6. *In vivo anti-metastasis therapy*

To explore the anti-tumor metastatic ability of different nano-formulations, 4T1 cells (1×10^6 cells/mouse) were subcutaneously injected into Balb/c female mice to establish an ectopic mouse tumor model. 4T1 cells (2×10^5 cells/mouse) were intravenously injected into each mouse 6 d later, and the mice were grouped ($n = 3$) and treated with various agents (saline, free IR-780, free IR+AT, IR@BSA, IR/AT@HPOC or M1-IR/AT@HPOC (2.5 mg/kg of IR-780 and ATRA)) the next day. The dosage and times of administration were consistent with the antitumor experiment. When the treatment ended, the lungs of the mice were dissected for recording the metastatic lesion number and H&E staining [40].

2.7. *In vivo long-term immune memory effects*

As M1-IR/AT@HPOC exhibited potent antitumor effects and elicited rapid systemic immune responses, we further established the recurrent and rechallenged tumor models to explore the long-term immune memory effect. Mouse ectopic models were established according to the protocol approach described in the anti-metastatic tumor research and tumor-bearing mice were treated with the same dosing regimen. About 90% of residual tumors were excised on Day 7 post-injection treatment and the treated mice were intravenously infused with 4T1 cells (2×10^5 cells/mouse) to establish

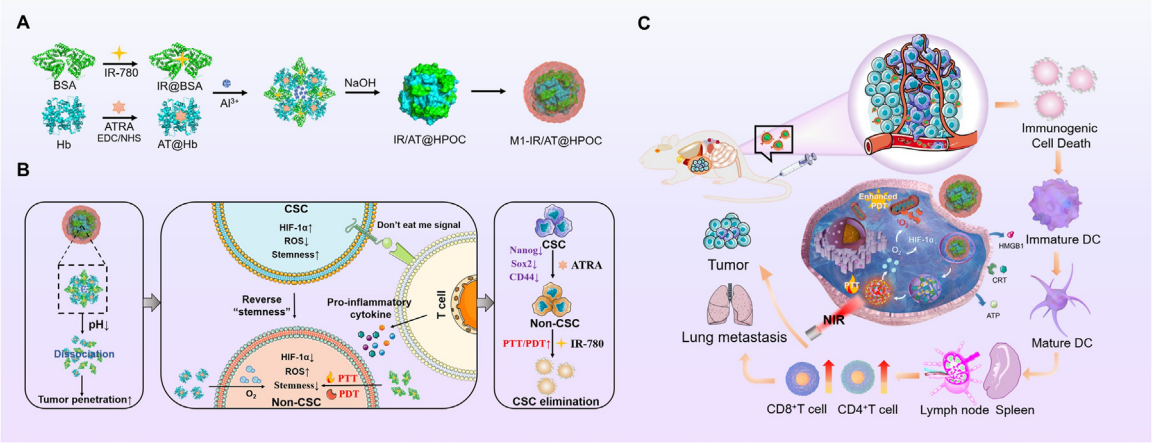

Scheme 1 – Schematic diagram of M1-IR/AT@HPOC and its inhibition of CSCs and activation of antitumor immune response. (A) Preparation of IR@BSA, AT@Hb, IR/AT@HPOC and M1-IR/AT@HPOC. (B) Schematic showing how ATRA reverses the CSC phenotype to a non-CSC phenotype, thereby reducing tumor "stemness" and boosting antitumor immunity. (C) Schematic illustration of combination therapy with PTT/PDT and differentiation induction and the enhancement of antitumor immunity: M1-IR/AT@HPOC triggers ICD, which subsequently promotes antigen release and activates T lymphocytes.

the rechallenged tumor model. After 14 d, the spleens were harvested and pressed gently using a syringe piston to obtain a single-cell suspension solution. The proportions of T_{EM} ($CD3^+CD8^+CD62L^-CD44^+$) were isolated and analyzed by flow cytometry [41,42].

2.8. *Statistics*

All data were processed by Graphpad prism 7.0. The statistical significance was analyzed using Students' *t*-test and two-way analysis of variance (ANOVA). All the results were presented as mean ± standard deviation (SD). Statistical significance was set at $^*P < 0.05$, $^{**}P < 0.01$ and $^{***}P < 0.001$.

3. Results and discussion

3.1. *Synthesis and characterization of M1-IR/AT@HPOC*

As shown in Scheme 1, M1-IR/AT@HPOC was synthesized and prepared in three steps. (1) preparation of IR@BSA and AT@Hb; (2) biomineralization; (3) polarization of M1-type macrophages and membrane camouflage. Specifically, Hb was first preconjugated with ATRA *via* the formation of amide bond to yield individual AT@Hb complexes with sizes around 20 nm. IR-780 could be anchored to BSA through the hydrophobic interaction between IR-780 and protein to form individual IR@BSA nanocomposites with sizes below 40 nm [32]. Then IR/AT@HPOC nanoparticles were obtained through a biomineralization process, which could integrate aluminum ions into IR@BSA and AT@Hb nanoparticles to form nanoclusters [28]. Finally, two components (M1 macrophage membranes and nanoclusters) are fused together to M1-IR/AT@HPOC with core-shell structure under the action of mechanical force. Transmission electron microscopy (TEM) images confirmed that the IR@BSA and AT@Hb were well-defined, with good monodispersity and typical spherical shape. Different from small particle-sized AT@Hb and IR@BSA, the mean diameter of IR/AT@HPOC was tested to be about 150 nm, indicating that the formed aluminum hydroxide had been integrated into IR/AT@HPOC nanoclusters. The image results also revealed that M1-IR/AT@HPOC showed a uniform "core-shell" structured morphology (Fig. 1A). These results confirmed that M1-IR/AT@HPOC was successfully prepared by the biomineralization method and successful coating of the cell membrane. Dynamic light scattering (DLS) data demonstrated that the hydrodynamic size of the IR@BSA was 30–40 nm, while the mean diameter of AT@Hb was approximately 20 nm (Fig. S1A). After biomineralization, the particle size of IR/AT@HPOC increased rapidly and larger protein nanoparticles were formed, with an average diameter of 150 nm. The M1-IR/AT@HPOC had a distinct core-shell structure with a hydrodynamic diameter of about 170 nm and an outer M1 membrane shell with 10 nm thickness, which agreed well with the previously reported thickness of the macrophage membrane (Fig. 1B and 1C) [43,44]. The surface charge of IR@BSA, AT@Hb, IR/AT@HPOC and M1-IR/AT@HPOC was verified by DLS and the corresponding zeta potentials were −12.2, −8.5, −16.1 and −23.3 mV, respectively. The zeta potential of the nanoparticles decreased from −16.1 to −23.3 after membrane coating, suggesting the successful M1 macrophage membrane coverage onto IR/AT@HPOC (Fig. S1B). Simultaneously, the successful M1 macrophage membrane camouflage could also be verified by SDS-PAGE (Fig. 1D).

We next investigated whether M1-IR/AT@HPOC could be stored for a long time. After lyophilization, M1-IR/AT@HPOC was instantly redissolved in deionized water with no apparent size change, showing good lyophilization stability. In addition, the lyophilized nanoparticles can also be well dispersed in PBS and 10% serum solution, with no significant change in particle size after 7-d incubation, indicating excellent stability under physiological conditions (Fig. S1C and S1D).

The loading capacities of ATRA and IR-780 in the AT@Hb and IR@BSA formation were determined to be 4.32% (w/w) and

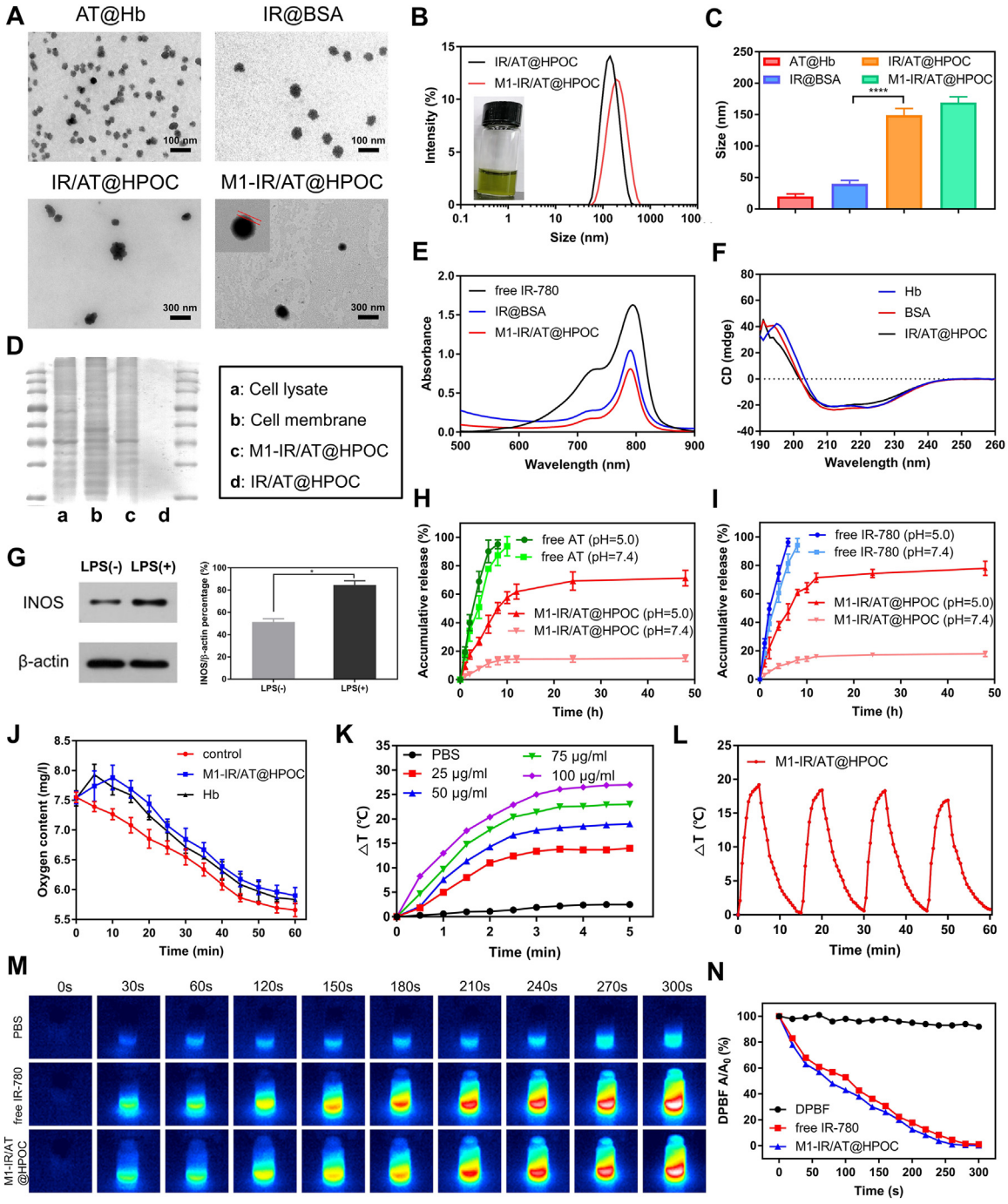

Fig. 1 – Synthesis and characterization of M1-IR/AT@HPOC. (A) TEM images of AT@Hb, IR@BSA, IR/AT@HPOC and M1-IR/AT@HPOC. (B) Size distribution of IR/AT@HPOC and M1-IR/AT@HPOC. (C) Diameter of AT@Hb, IR@BSA, IR/AT@HPOC and M1-IR/AT@HPOC ($n = 3$). (D) SDS-PAGE analysis of cell lysate, cell membrane, M1-IR/AT@HPOC and IR/AT@HPOC. (E) UV–vis absorption spectroscopy of free IR-780, IR@BSA and M1-IR/AT@HPOC. (F) CD spectra of Hb, BSA and IR/AT@HPOC. (G) Western blot of iNOS expression in macrophage membrane with or without LPS treatment and quantitative analysis of iNOS expression. (H) Acid sensitive release of ATRA from free ATRA and M1-IR/AT@HPOC ($n = 3$). (I) Acid sensitive release of IR-780 from free IR-780 and M1-IR/AT@HPOC ($n = 3$). (J) Changes in oxygen consumption by 4T1 cells in cell culture medium with M1-IR/AT@HPOC or Hb. (K) Temperature changes of M1-IR/AT@HPOC solution of different concentration exposed to NIR laser. (L) Temperature change profile of M1-IR/AT@HPOC solution (50 μg/ml) exposed to NIR laser after four cycles. (M) Infrared thermal images of PBS, free IR-780 and M1-IR/AT@HPOC solutions exposed to NIR laser. (N) ROS of free IR-780 and M1-IR/AT@HPOC exposed to NIR laser using DPBF.

6.13% (w/w), while the encapsulation efficiencies of ATRA and IR-780 were 90.3% and 87.11% detected by HPLC and UV–vis-NIR absorbance spectra, respectively (Table S1 and S2).

Free IR-780 had an obvious absorption peak at 784 nm detected by UV–vis spectrophotometer. Meanwhile, the absorption peak intensity of IR@BSA was lower than that of free IR-780, which proved that IR-780 encapsulated in BSA reduced part of the absorbance. The absorbance intensity of M1-IR/AT@HPOC was lower than that of IR@BSA, indirectly proving the successful modification of the cell membrane in M1-IR/AT@HPOC (Fig. 1E) [45].

The effects of physical loading and chemical bonding on the secondary structure of BSA and Hb were analyzed by circular dichroism (CD) spectrum. As shown in Fig. 1F, compared with BSA and Hb, the typical characteristic peak of α-helix (190–195 nm) and the negative ellipticity at 217 nm have no significant changes during the preparation process of IR/AT@HPOC, meaning that the secondary structures of BSA and Hb were intact, and the basic biological functions were not affected.

Macrophage biomarker levels such as F4/80, CD80 and iNOS were assessed to further test macrophage polarization. Macrophages can polarize into M1 phenotype under the stimulation of LPS, and the expression of markers (CD86 and F4/80) on the surface of M1 macrophages increased significantly from 49% to 73.2% (Fig. S1E). Successful polarization of M1-type macrophages was also demonstrated by the increased expression of iNOS (Fig. 1G).

Owing to the pH-responsiveness of biomineralized nanocarriers, the pH-responsive release of ATRA and IR-780 from M1-IR/AT@HPOC was investigated at different pH (5.0 and 7.4). The release of ATRA and IR-780 from M1-IR/AT@HPOC displayed a sustained pattern compared with free drugs. The M1-IR/AT@HPOC could release about 73.7% and 16.2% ATRA at pH 5.0 and 7.4, respectively (Fig. 1H). Similarly, the release of IR-780 can reach 79.7% and 17.8% at pH 5.0 and 7.4, respectively (Fig. 1I). This is mainly due to the acidity-induced dissociation of aluminum hydroxide in M1-IR/AT@HPOC into individual albumin-based complexes, thus accelerating the drug release. To explore the pH sensitivity of these nanoparticles, the incubation of M1-IR/AT@HPOC was performed at different pH conditions. TEM images revealed no significant change in the morphology of M1-IR/AT@HPOC at pH 7.4, indicating that M1-IR/AT@HPOC was quite stable under physiological conditions. It was found that the overall structure of M1-IR/AT@HPOC degraded in the acidic TME of pH 6.8, while M1-IR/AT@HPOC dissociated into ultrasmall species under the condition of pH 5.0. Furthermore, DLS data also demonstrated that the particle size of M1-IR/AT@HPOC decreased significantly under acidic conditions, indicating that aluminum hydroxide in M1-IR/AT@HPOC could undergo responsive degradation under acidic conditions to release small particle size protein drugs, which was conducive to tumor deep penetration (Fig. S1F). These results suggest that M1-IR/AT@HPOC could maintain its stability during blood circulation and release these two substances in response to dissociation under acidic TME for effective tumor treatment.

Since Hb acted as an oxygen-binding protein under physiological conditions, we envisaged that oxygen could be encapsulated and retained in M1-IR/AT@HPOC, and it was then transported to tumor sites to alleviate tumor hypoxia. For this purpose, the oxygen consumption rate (OCR) was determined by measuring the change in oxygen content in the sealed cell culture medium. Due to the oxygen consumption of 4T1 cells, the oxygen concentration in the control group decreased significantly with time. When 4T1 cells were incubated with M1-IR/AT@HPOC or Hb, the oxygen concentration first increased and then decreased, implying that the oxygen loaded in the nanocarriers or Hb was released during the initial phase. The decreased oxygen concentration in the later period was attributed to the consumption of oxygen by 4T1 cells. This results indicated that the both M1-IR/AT@HPOC and Hb could carry oxygen to alleviate the hypoxia of tumor site (Fig. 1J) [46].

3.2. *In vitro PTT and PDT evaluation*

To evaluate the photothermal performance, the M1-IR/AT@HPOC solutions with different concentrations were exposed to an 808 nm laser, and the experimental results demonstrated that M1-IR/AT@HPOC exhibited concentration-dependent photothermal properties (Fig. 1K). When the irradiation time increased from 0 to 60 s, free IR-780 underwent degradation and photo-bleaching when exposing to NIR laser, leading to a great decrease in the absorbance of free IR-780. Nevertheless, the UV–vis absorption spectrum of M1-IR/AT@HPOC decreased slightly mainly because the outer coating of M1-IR/AT@HPOC and the protective effect of protein carriers could effectively reduce the photobleaching phenomenon of IR-780 itself (Fig. S2). Furthermore, no significant changes in the photothermal properties of M1-IR/AT@HPOC were observed after four “on/off” irradiation cycles, indicating that M1-IR/AT@HPOC possessed ideal photothermal properties stability (Fig. 1L). According to infrared thermal images, the temperature of the M1-IR/AT@HPOC sample increased sharply after laser irradiation, exhibiting a photothermal efficiency similar to that of the free IR-780 (Fig. 1M). These results suggest that the preparation of nano-carriers and the camouflage of cell membranes have negligible effects on the PTT effect of IR-780. Photothermal conversion efficiency is a parameter used to evaluate the PTT properties of materials. The calculated photothermal conversion efficiency of IR/AT@HPOC and M1-IR/AT@HPOC was 19.98% and 22.34%, which might be attributed to the non-radiative relaxation from the excitons in the excited IR-780 (Fig. S3) [47,48].

To study the photodynamic performance of nanodrugs, DPBF was used as a probe to measure the absorbance at various time points by adding free IR-780 or M1-IR/AT@HPOC (equivalent to 5 μg/ml IR-780). Fig. 1N manifested that M1-IR/AT@HPOC generated almost the same singlet oxygen content as free IR-780 at the same dose, proving that both free IR-780 and M1-IR/AT@HPOC showed similar ROS generation efficiency.

3.3. *Characterization of stemness-related property and therapeutic effect of nano-preparations*

Different from the adherent growth mode, 4T1 cells grew in suspension in serum-free medium to form three-dimensional

cell spheres. On the first day of culture, the spheroids began to form, and the spheroids formed completely on Day 3 to 4, and finally formed a solid structure composed of many cells tightly bound by the Day 7. After several successive generations of culture, the compactness and volume of cell spheres also increased. After removed the growth factor and induced by serum for 48 h, the suspended cell spheres could quickly restore their differentiation ability and continuously adhere to the bottle wall to form adherent cells (Fig. S4).

To examine the proportion of SPs in tumor cells, the 4T1 cell line was stained with Hoechst 33,342 dye and SPs were identified by their characteristic fluorescence spectrum. Both the verapamil group and the ATRA group could significantly reduce the ratio of stemness-related cells from 2.96% to 0.79% and 0.83% compared to the no-verapamil group (Fig. 2A).

ATRA can inhibit the proliferation of cancer cells through various pathways, including induction of differentiation, apoptosis and cell cycle regulation. Therefore, we performed cell cycle assays on ATRA-treated cells. Flow cytometry results showed that the differentiation-inducing effect of ATRA was concentration-dependent. ATRA of 15 μg/ml could significantly increase the G1 phase from 35.55% to 52.35%, and reduce the S phase from 50.41% to 28.82% (Fig. 2B and S5).

We evaluated the combined effects of ATRA and IR-780 in the clearance of CSCs *in vitro*. ATRA/IR-780 (m:*m* = 1:1) treatment caused higher levels of cytotoxicity in CSCs (Fig. 2C). Besides, continuing to increase the proportion of ATRA did not significantly increase the killing effect of CSCs. Therefore, we chose ATRA/IR-780 (m:*m* = 1:1) as the dosing ratio for subsequent experiments.

The $CD44^+CD24^-$ marker, identified as a marker of CSCs in breast cancer, was commonly used to characterize the stemness of 4T1-induced mammospheres. To investigate the differentiation-inducing effect of ATRA, untreated 4T1 cells and ATRA-treated mammospheres were analyzed by flow cytometry to examine changes in the ratio of $CD44^+/CD24^-$ cell populations. Experimental data showed that 33.6% of $CD44^+CD24^-$ cells were highly detected in mammospheres, but very rarely (less than 3%) in untreated 4T1 cells (two-dimensional culture). Additionally, we observed a significant decrease in the ratio of $CD44^+/CD24^-$ cell populations with increasing ATRA concentrations (Fig. 2D). Meanwhile, the changes in the percentage of $CD44^+/CD24^-$ cell populations in mammospheres were examined after treatment with different preparations. The results revealed that the IR-780 could reduce the $CD44^+/CD24^-$ cell population ratio to a certain extent, while the addition of ATRA could significantly reduce the stemness of mammospheres, from 37.1% to 23.0%. The M1-IR/AT@HPOC group exhibited the strongest inhibition of the $CD44^+/CD24^-$ cell population, ranging from 37.1% to 12.8%. These data suggest that ATRA could not only differentiate and induce CSCs to reduce their stemness characteristic, but also facilitate the killing effect of IR-780 on CSCs, thereby reducing the proportion of CSCs through multiple ways (Fig. S6).

CSCs treated with different preparations were examined by western blotting method for differentiation-inducing effects of ATRA and expression on typical stemness-related proteins including OCT-4 and SOX2. The experimental results demonstrated that ATRA and AT@Hb-treated tumorspheres showed significant down-regulation in the expression of OCT-4 and SOX2, thus proving the differentiation-inducing effect of ATRA on tumor stem cells (Fig. S7A-S7C). As shown in Fig. 2E, the IR@BSA group decreased the expression of OCT-4 and SOX2 in CSCs by improving the hydrophobicity and photostability of IR-780 compared to the free IR-780 group. While the tumor spheres treated with M1-IR/AT@HPOC showed the lowest OCT-4 and SOX2 expression levels, suggesting that cell membrane camouflage could enhance therapeutic efficacy by increasing uptake of tumor cells (Fig. S7D and S7E). Overall, ATRA-promoted CSC differentiation could significantly increase their sensitivity to phototherapy, where “adaptation” to CSCs *via* ATRA modulation was beneficial to maximize the therapeutic effect [6].

Furthermore, the effect of cytotoxicity produced by different formulations on the proliferative capacity of 4T1 cells was determined by clonogenic assays. 4T1 colony formation images showed that control group had the highest clonogenic capacity, while the M1-IR/AT@HPOC treated group exhibited the least cloning (Fig. S8), indicating that M1-IR/AT@HPOC could extremely inhibit the colony formations of 4T1 cells by the cytotoxicity of IR-780 and the differentiation ability of ATRA on CSCs (Fig. 2F). The ability of mammosphere formation under suspension culture conditions has been identified as a stemness-related feature in 4T1 cells. Therefore, the mammosphere formation study was also performed to determine the effect of different nanomedicines on the ability of tumorsphere formation (Fig. S8). Extensive tumor sphere formation was observed in the control group, whereas phototherapy and differentiation-mediated treatment reduced tumor sphere formation. IR/AT@HPOC significantly decreased the number and size of mammospheres, proving that combined differentiation therapy and phototherapy could inhibit the formation capability of tumor spheres. The tumor spheres formed after M1-IR/AT@HPOC treatment were greatly reduced, suggesting that targeting effect of the M1 macrophage membrane could promote nanoparticle uptake (Fig. 2G).

3.4. *Cellular uptake and tumorsphere penetration*

The cellular uptake efficacy of different preparations in 4T1 murine breast cancer cells was evaluated by CLSM. The confocal fluorescence imaging (Fig. S9) revealed strong IR-780 fluorescence in 4T1 cells incubated with M1-IR/AT@HPOC, while 4T1 cells in free IR-780 group showed weaker IR-780 fluorescence due to its lower cellular uptake efficiency. Also from the data of flow cytometry (Fig. S10A and S10B), we could observe a small amount of M1-IR/AT@HPOC was taken up by 4T1 cells at 1 h, and after prolonged incubation time, strong IR-780 fluorescence was detected in the cells, demonstrating that the cellular uptake of M1-IR/AT@HPOC was time-dependent. The cellular uptake efficiency of CSCs after being treated with different nanoparticles was then studied. And according to the flow cytometry data (Fig. 2H), the mean fluorescence intensity of the IR@BSA and IR/AT@HPOC group was significantly greater than free IR-780 and free IR+AT groups. This could be due to the fact that nanometrization contributed to the endocytosis of cells. M1-IR/AT@HPOC-

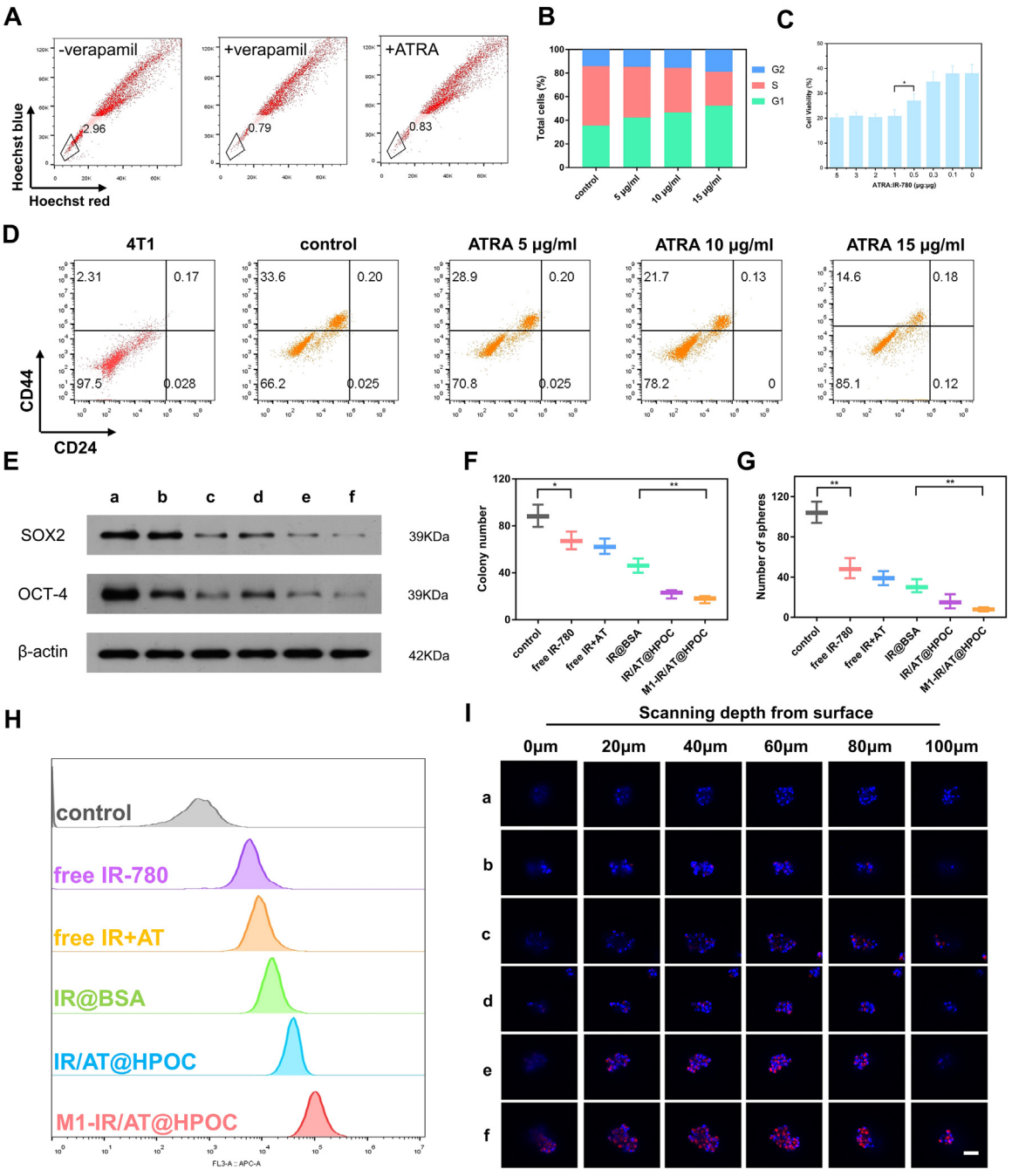

Fig. 2 – Stem cell characterization and cellular uptake. (A) Representative images of flow cytometric sorting of 4T1 cells treated with verapamil or ATRA. (B) Analysis of cell cycle phases in 4T1 cells after co-incubation with ATRA at 5, 10 or 15 μg/ml for 24 h. (C) Cell viabilities of CSCs treated with ATRA and IR-780 at different molar ratios under NIR laser irradiation. (D) The expression of $CD44^{+}CD24^{-}$ markers in CSCs and 4T1 cells after co-incubation with ATRA of different concentrations. (E) Western blot analysis of SOX2 and OCT-4 expression from CSCs after treatment with a: control, b: free IR-780, c: free IR+AT, d: IR@BSA, e: IR/AT@HPOC and f: M1-IR/AT@HPOC. (F) The corresponding colony number after culture with different formulations ($n = 3$). (G) The corresponding tumorsphere number after culture with different formulations ($n = 3$). (H) Flow cytometric analysis of CSCs after culture with different formulations ($n = 3$). (I) Confocal images of 4T1 mammospheres after co-incubation with different formulations for 4 h. Scale bar: 100 μm.

treated cells exhibited stronger IR-780 fluorescence intensity compared with IR/AT@HPOC-treated cells, suggesting that cell membrane camouflage could be utilized to effectively increase the uptake of nanoparticles through active targeting effects.

To examine the ability of nanocarriers to enter the deeply seated CSCs, the permeability of different formulations into mammospheres was investigated through CLSM. After treatment with free IR-780, only little red fluorescence was detected in the 4T1 mammospheres across each equatorial section in Fig. 2I. The fluorescence distribution in the middle part of the mammospheres indicated that free IR+AT exhibited stronger penetration than free IR-780, which may be attributed to the reversal effect of ATRA on CSCs for increasing the uptake of IR-780. IR/AT@HPOC could enhance the penetration of nanoparticles in the CSCs to a certain extent, which may be due to the decomposition of nanoclusters into small-sized protein drugs in the acidic microenvironment. M1-IR/AT@HPOC group increased the uptake of nanomedicines through the affinity of M1 macrophage membranes for tumor cells and therefore demonstrated the strongest penetration ability (Fig. S10C) [49].

3.5. *Cytotoxicity evaluation*

To corroborate the synergistic anti-tumor effect, CCK-8 assay was applied to evaluate the cytotoxicity of 4T1 cells and CSCs treated with different preparations. In the absence of laser irradiation, cells treated with low concentration of M1-IR/AT@HPOC group had a cell survival rate close to 100%. Even at a high dose of IR-780 (10 μg/ml), cell viability in the M1-IR/AT@HPOC group was maintained above 50%. For the irradiated group of M1-IR/AT@HPOC, the cell viability decreased greatly, suggesting that NIR laser irradiation was necessary to evoke the PTT and PDT effects of IR-780 (Fig. S11A). As depicted in Fig. 3A, the IC_{50} values of free IR-780, free IR+AT and IR@BSA groups were 7.723 μg/ml, 5.918 μg/ml and 3.745 μg/ml with progressively increasing cytotoxicity, which may be influenced by the level of cellular uptake. Notably, IR/AT@HPOC exhibited higher toxicity (IC_{50} = 2.09 μg/ml), which further increased after M1 macrophage membrane camouflage with IC_{50} of 1.663 μg/ml, probably due to the targeting effect of membrane modifications. The combination of differentiation therapy and phototherapy on eliminating CSCs *in vitro* were next evaluated. IR@BSA had a good anticancer effect on 4T1 cells through an efficient PTT/PDT effect, and IR@BSA could kill almost all 4T1 cells at a concentration of 20 μg/ml. However, the cell viability of CSCs remained around 50% after IR@BSA treatment at this concentration, suggesting that CSCs were resistant to photothermal and photodynamic treatments in the absence of differentiation-inducing treatment, thus leading to the low treatment efficiency. With the involvement of AT@Hb, the cell viability of CSCs significantly decreased with increasing IR/AT@HPOC concentration compared to the IR@BSA group, which was due to the differentiation effect of ATRA loading (Fig. S11B).

To explore whether the anti-proliferative activities of different formulation groups on 4T1 cells and CSCs were accompanied by an increase in apoptosis, the flow cytometry was performed using Annexin V/PI cell assay method. As exhibited in Fig. 3C, slight apoptosis was observed in the 4T1 cells and CSCs in free IR-780 group with NIR irradiation (11.2% and 8.15%). The laser-treated IR-780-containing formulations including IR@BSA and IR/AT@HPOC induced obvious apoptosis/necrosis of 4T1 cells and CSCs. Compared with other groups, M1-IR/AT@HPOC produced the highest apoptosis/necrosis rate in 4T1 cells and CSCs with apoptosis rates of 44.2% and 40.2%. To study the molecular mechanism of apoptosis, the levels of apoptotic marker caspase-3 activation were detected. As shown in Fig. 3B, different formulations activated caspases-3 in a dose-dependent manner. The IR-780-containing formulations could prominently increase caspase-3 levels in contract with free drug groups. In conclusion, the combination of phototherapy and differentiation therapy can induce caspase-3 expression as well as accelerate apoptosis of tumor cells and CSCs.

In this work, the inhibition activities of different preparations on 4T1 cells and CSCs were also evaluated through Calcein AM/PI double staining method [50]. As illustrated in Fig. 3D, 4T1 cells and CSCs in control groups exhibited almost no red signal, indicating that the control group induced negligible cell death. The live/dead assays after treatment with different formulation groups clearly demonstrated the synergistic phototherapy and differentiation-inducing effects of the nanodrugs on 4T1 cells and CSCs. Compared with IR/AT@HPOC, M1-IR/AT@HPOC induced more cell death, which may be attributed to increased cellular uptake.

3.6. *ROS generation*

The intracellular ROS generation in different preparations was examined by DCFH-DA staining method and monitored by CLSM. Fluorescence imaging showed that free IR-780 and free IR+AT groups triggered nearly no ROS production, while the preparation groups showed abundant green fluorescence signals than the free drug groups. The phenomenon might arise from the fact that nanocarriers could promote the uptake efficiency of the IR-780. Furthermore, the cells followed by incubation with IR/AT@HPOC and M1-IR/AT@HPOC exhibited a degree of fluorescence increase compared with other groups, indicating that oxygen carried by Hb could enhance the generation of intracellular ROS by relieving tumor hypoxia (Fig. 3E).

3.7. *Subcellular distribution*

Nanodrugs captured by lysosomes are easy to be degraded under the action of the acid environment and enzymes, leading to reduced efficacy or even loss of efficacy. Therefore, timely lysosome escape is of paramount importance for the efficacy of nanomedicine. The biomineralization method can utilize the “proton sponge” effect to destroy the lysosomal membrane and provoke the lysosome escape. The lysosome localization of M1-IR/AT@HPOC at different times was confirmed in the 4T1 cells by co-staining with M1-IR/AT@HPOC and Lyso-Tracker Green. After 1 h of incubation, almost all internalized nanoparticles co-localized with

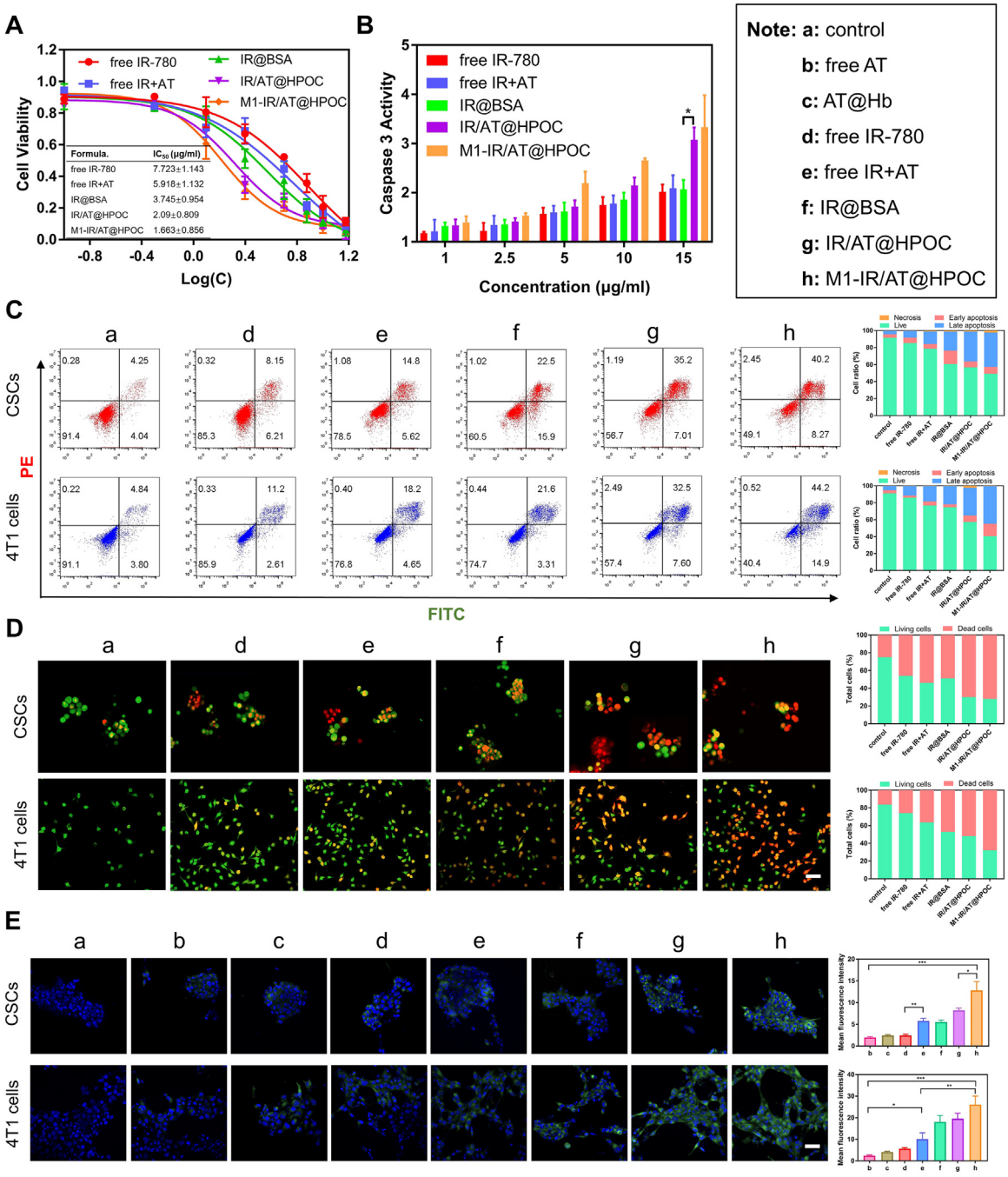

Fig. 3 – *In vitro* cytotoxicity assays. (A) Cell viabilities of 4T1 cells after co-incubation with different formulations under NIR laser irradiation ($n = 6$). (B) Caspase 3 activity of 4T1 cells in different groups under NIR laser irradiation ($n = 3$). (C) Apoptosis analysis of CSCs and 4T1 cells after different treatments under NIR laser irradiation and quantitative comparison. (D) Live and dead cell staining analysis of CSCs and 4T1 cells after different treatments under NIR laser irradiation and quantitative comparison. Scale bar: 100 μm. (E) Confocal images of ROS generation in CSCs and 4T1 cells after different treatments under NIR laser irradiation and quantitative comparison. Scale bar: 100 μm.

lysosomes, and the Pearson correlation coefficient was as high as 0.816, demonstrating that M1-IR/AT@HPOC was distributed into lysosomes. In contrast, after 4 h incubation of M1-IR/AT@HPOC, most of M1-IR/AT@HPOC escaped from lysosomes with a Pearson correlation coefficient of 0.543, which was mainly attributed to its pH-sensitive properties of aluminum hydroxide in M1-IR/AT@HPOC (Fig. 4A).

Mitochondria are composed of a phospholipid bilayer membrane structure with proton pumps to form a proton gradient, so as to establish a more negative mitochondrial membrane potential inside. Hence, lipophilic and cationic

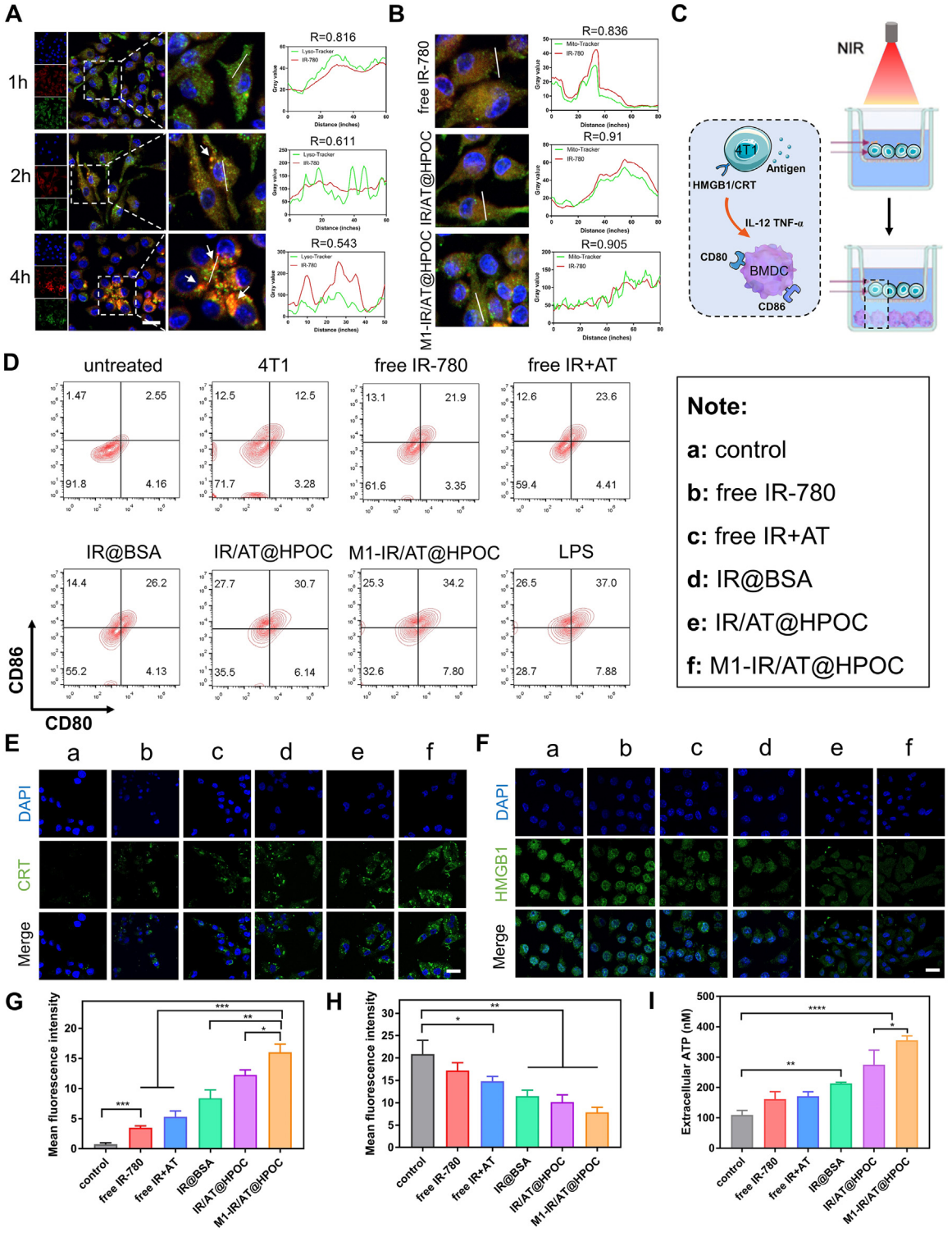

Fig. 4 – Subcellular distribution and immune activation. (A) Confocal images of M1-IR/AT@HPOC at different times wherein nucleus was stained in blue, IR-780 was exhibited in red, and lysosome was stained in green. The colocalization of IR-780 or Lyso-tracker fluorescence curve along the white line. Scale bar: 20 μm. (B) Confocal images of 4T1 cells incubated with free IR-780, IR/AT@HPOC or M1-IR/AT@HPOC wherein nucleus was stained in blue, IR-780 was exhibited in red, and mitochondria was stained in green. The colocalization of IR-780 or Mito-tracker fluorescence curve along the white line. (C) Schematic illustration of transwell system detecting DC maturation. (D) Flow cytometric analysis of the maturation of DCs after 4T1 cells after culture with different formulations. (E) Confocal images of CRT exposure in different treatment groups exposed to NIR laser. Scale bar: 50 μm. (F) The release of HMGB-1 in different treatment groups exposed to NIR laser. Scale bar: 50 μm. (G) Quantitative analysis of CRT exposure. (H) Quantitative analysis of HMGB1 release. (I) Extracellular ATP release from 4T1 cells in different treatment groups exposed to NIR laser ($n = 3$).

compounds favor accumulation within mitochondria. IR-780 molecules possess these characteristics to promote transportation to mitochondria. The mitochondrial targeting properties of free IR-780, IR/AT@HPOC, M1-IR/AT@HPOC were then extensively studied. We observed that the IR-780 fluorescence signal and mitochondria also co-localized well after 4 h of incubation, with Pearson correlation coefficients of 0.836, 0.91 and 0.905, respectively (Fig. 4B and S12). The experimental results verified the excellent mitochondrial targeting properties of IR-780, and the IR-780 molecules could be easily escaped from lysosomes and transported to mitochondria.

To further clarify the mitochondrial changes induced by M1-IR/AT@HPOC, the decrease of mitochondrial membrane potential was studied with a JC-1 fluorescent probe. When IR-780 acts on mitochondria to disrupt membrane integrity, mitochondria depolarize with reducing JC-1 aggregates of red fluorescence and increasing JC-1 monomers of green fluorescence [51]. From the confocal image, the control group exhibited a normal state of mitochondria with much less punctated green fluorescence than red fluorescence. For the laser-treated IR-780-containing groups, decreased red fluorescence and increased green fluorescence were observed. The flow cytometry results showed the intensity ratio of JC-1 aggregates to JC-1 monomers. Compared with the control group, the green fluorescent signal of JC-1 increased from 3.00% to 30.7%, suggesting that the M1-IR/AT@HPOC-treated group caused the most severe mitochondrial damage (Fig. S13). Overall, our M1-IR/AT@HPOC could trigger lysosome escape after entering tumor cells, release active compounds into the cytoplasm, then target mitochondria and induce programmed cell death through mitochondrial dysfunction [52].

3.8. *Enhanced oxygen generation*

Considering the oxygen-carrying capacity of Hb reported previously, the potent photodynamic effect induced by M1-IR/AT@HOPC may be explained by the alleviating effect of Hb on tumor hypoxia [53]. As shown in Fig. S14 and S15, Hb-containing treatment groups apparently quenched the red fluorescence of the oxygen probe $[Ru(dpp)_3]Cl_2$ in contrast to the control group, confirming the intracellular oxygen-carrying capacity of Hb. Conversely, the free IR-780 and IR@BSA groups consumed oxygen due to the production of PDT, which in turn led to aggravated tumor hypoxia. The fluorescence signal (red) was similar in the M1-IR/AT@HPOC group and the IR/AT@HPOC group, which was due to the dual effects of oxygen-carrying of Hb and oxygen consumption of PDT.

3.9. *Cell invasion assay*

We further evaluated whether M1-IR/AT@HPOC effectively inhibited tumor cell invasion and metastases. As shown in Fig. S16, the statistical calculation of the gap distance indicated that free IR-780 significantly reduced the migration ability of 4T1 cells from 42.6% to 36.5% compared with PBS as a control. Meanwhile, the cell migration rates of the IR/AT@HPOC and M1-IR/AT@HPOC groups were 26.0% and 20.9%, respectively, which were obviously lower than control group [54]. The results indicated that M1-IR/AT@HPOC reduced the invasive ability of tumor cells, suggesting the ability to inhibit tumor metastasis.

3.10. *Immune activation in vitro*

The maturation of DCs through the M1-IR/AT@HPOC-induced ICD of 4T1 cells was verified by using the transwell system (Fig. 4C). After different treatments of 4T1 cells in the upper chamber, DCs in the bottom chamber were collected and investigated by flow cytometry to assess the stimulation of DCs by tumor antigens produced by 4T1 cells. Compared with the untreated group and the single-4T1 cell group, the treatment group significantly increased the maturity of DCs due to extensive cell death, and the maturation of DCs in the M1-IR/AT@HPOC group increased up to 34.2%, which was similar to LPS group (37.0%). Significantly, IR/AT@HPOC treatment could enhance the maturation of DCs with the maturation rate of 30.7%, which was 4.5% higher than the IR@BSA group. The results of this experiment confirmed the increased maturation of DCs due to the cooperation of phototherapy and differentiation therapy. Our data indicated that M1-IR/AT@HPOC mediated-combined phototherapy and differentiation therapy could activate more DC *in vitro* than single phototherapy to further enhance anti-tumor immune response (Fig. 4D) [55].

Different formulations containing IR-780 trigger the ICD effect by inducing the surface translocation of CRT, the release of ATP molecules and HMGB1 from the nucleus into the extracellular environment [56]. Cells treated with free IR-780 exhibited a slight exposure level of CRT as visualized by Fig. 4E. Fluorescence imaging detection confirmed that compared with the control group, preparation groups containing IR-780 could significantly strengthen green fluorescence signal of CRT on the cell surface, stating that the PTT/PDT had superior performance in destroying tumors and enhancing tumor cell immunogenicity (Fig. 4G). In addition, 4T1 cells treated with IR@BSA had limited HMGB1 (Fig. 4F and 4H) and ATP (Fig. 4I and S17) release, while obviously ATP and HMGB1 release were observed in IR/AT@HPOC group, suggesting that ATRA-mediated phototherapy could promote induction of ICD. This was mainly because ATRA could strengthen the cytotoxicity of IR-780 by reducing the proportion of CSCs, thereby improving the ICD effect.

3.11. *In vitro biosafety evaluation*

The hemolysis assay confirmed the good biosafety of M1-IR/AT@HPOC for *in vivo* utilization. With the increase of sample concentration, the hemolysis percentage of erythrocytes was all below 5%, indicating that M1-IR/AT@HPOC had no obvious interference with red blood cells and had good *in vivo* safety (Fig. S18).

3.12. *Tumor-targeted accumulation and oxygen delivery efficiency*

Considering previous encouraging performance of M1-IR/AT@HPOC *in vitro*, we further investigated the tumor

targeting efficiency of M1-IR/AT@HPOC *in vivo* through an IVIS fluorescence imaging system. As illustrated in Fig. 5A, the fluorescence intensity of tumor tissues in free IR-780 group peaked at 12 h post-injection, thereafter, the fluorescence intensity of IR-780 started to diminish. In contrast, the fluorescence intensity in the tumor site of nano-preparation groups was consistently enhanced within 24 h. Compared with the free IR-780 group, the IR/AT@HPOC group showed significantly and consistently stronger fluorescence at the tumor site over a period of 24 h, indicating that the fabricated nanoplatforms have obvious long-term circulation and tumor accumulation ability. In addition, the M1-IR/AT@HPOC group exhibited the strongest tumor fluorescence signal, which was associated with the M1 macrophage membrane-mediated tumor recruitment effect (Fig. 5C). The *ex vivo* fluorescence imaging of isolated tissues displayed a consistent phenomenon (Fig. 5B). Tumors and main organs were collected from mice 24 h after drug administration for *ex vivo* imaging. The *ex vivo* images demonstrated almost no fluorescence in the tumor treated with free IR-780 and fluorescence was hardly observed in lungs, spleens, and hearts. There was obvious increased IR-780 fluorescence in the tumor site of IR/AT@HPOC group, while M1-IR/AT@HPOC retained strong fluorescence in tumor tissues, indicating superior tumor accumulation of nano-preparations. Semiquantitative biodistribution results demonstrated that compared to the free IR-780 group, M1-IR/AT@HPOC was retained the longest in the liver, followed by the tumor tissue (Fig. 5D). Taken together, these results showed that M1-IR/AT@HPOC resulted in prolonged tumor retention and outstanding tumor accumulation due to its inherent tumor homing and deep penetration properties.

M1-IR/AT@HPOC has a strong tumor-targeted oxygen supply capacity due to the oxygen carried by Hb, while the larger-sized natural red blood cells cannot penetrate deeply into the tumor interstitium. Therefore, to visualize tumor penetration and oxygenation of M1-IR/AT@HPOC, the photoacoustic imaging was performed 8 h after administration to measure the Hb (represented hypoxia, 700 nm) and HbO_2 (represented normoxia, 850 nm) (Fig. 5E). Before the injection of saline, IR/AT@HPOC and M1-IR/AT@HPOC, the tumor sites of mice exhibited high levels of Hb photoacoustic intensity, which was mainly attributed to the hypoxia of the tumor sites. After 8 h, the targeted oxygen supply of IR/AT@HPOC and M1-IR/AT@HPOC significantly enhanced the PA signal of HbO_2 at the tumor site. Comparatively, the most top PA signal of HbO_2 could be observed in M1-IR/AT@HPOC group, which presented that the tumor hypoxia was effectively alleviated (Fig. 5F) [57]. Besides, tumor hypoxia can also be characterized by changes in the expression level of HIF-1α. The mean fluorescence intensity of HIF-1α marker showed that mice treated with IR-780 resulted in increased tumor hypoxia, mainly due to the increased oxygen consumption to the tumor site by the generated PDT. It should also be noted that IR/AT@HPOC and M1-IR/AT@HPOC groups could alleviate tumor hypoxia through the oxygen-carrying ability of Hb, which had been verified by down-regulation of HIF-1α expression (Fig. 5G and S19A).

3.13. *In vivo thermal imaging and PDT efficiency*

The thermal imaging of tumor-bearing mice receiving different treatments was assessed by an infrared thermal camera (Fig. 5H and S20). The thermal imaging data showed that the local tumor temperature of saline group increased by 4.2 °C, while it increased by 9.3 °C and 11.6 °C in the free IR-780 and free IR+AT groups during the laser irradiation. In IR/AT@HPOC group, the tumor exposed to laser irradiation demonstrated a maximum temperature increase of 17.8 °C. The tumor temperature in M1-IR/AT@HPOC-treated mice increased rapidly and reached 49.1 °C at 5 min, a value high enough to thermally ablate the tumor (Fig. 5I). These data suggest that the effective accumulation at tumor sites and the excellent photostability of M1-IR/AT@HPOC could produce significant photothermal effects for cancer therapy.

Next, the PDT effect of M1-IR/AT@HPOC on tumor sites in mice was explored through a DCFH-DA staining method. The obvious fluorescence of ROS probe was found in the excised tumors of mice receiving IR-780-containing preparations after laser irradiation, indicating that IR-780 generated ROS through the PDT effect. For the M1-IR/AT@HPOC treated group, the strongest green fluorescence intensity was observed, which clearly proved that M1-IR/AT@HPOC exerted a potent PDT effect *in vivo* (Fig. 5J and S19B).

3.14. *In vivo anti-primary tumor therapy*

Afterward, the xenografted 4T1 tumor models were established to assess the antitumor efficacy of different preparations *in vivo*. When tumors closed to about 100 mm^3, mice were assigned randomly to eight groups and injected intravenously with different preparations including saline, free AT, AT@Hb, free IR-780, free IR+AT, IR@BSA, IR/AT@HPOC and M1-IR/AT@HPOC ($n = 5$). The IR-780-containing preparations were subjected to NIR laser irradiation for 5 min within 12 h after injection. Fig. 6A described the tumor growth curve of 4T1 tumor-bearing mice after treatments. The experimental results indicated that the tumor volume of saline group increased rapidly with the passage of time, while single ATRA and AT@Hb only moderately inhibited tumor growth. After treatment with the preparations containing IR-780, the growth of tumors in mice could be effectively inhibited, which indicated that PDT and PTT induced by IR-780 under NIR irradiation could effectively eliminate primary tumors in mice. Moreover, the relative tumor volume of IR/AT@HPOC group was much smaller than that of free IR+AT group, indicating that nano-preparations could improve the inhibitory effect of combination therapy on tumor growth. By sharp contrast, the M1-IR/AT@HPOC group was highly effective in inhibiting tumor growth by completely eradicating 86.98% of 4T1 tumors by combining phototherapy and differentiation induction therapy. Fig. 6B and E demonstrated the tumor volumes during 2 weeks of various treatments. The tumors in saline group grew rapidly during the treatment period from an initial size of about 100 mm^3 to 1700 mm^3. Interestingly, M1-IR/AT@HPOC significantly suppressed tumor growth in mice and shrank slightly at the end of treatment, which could also be found in Fig. 6D. According to

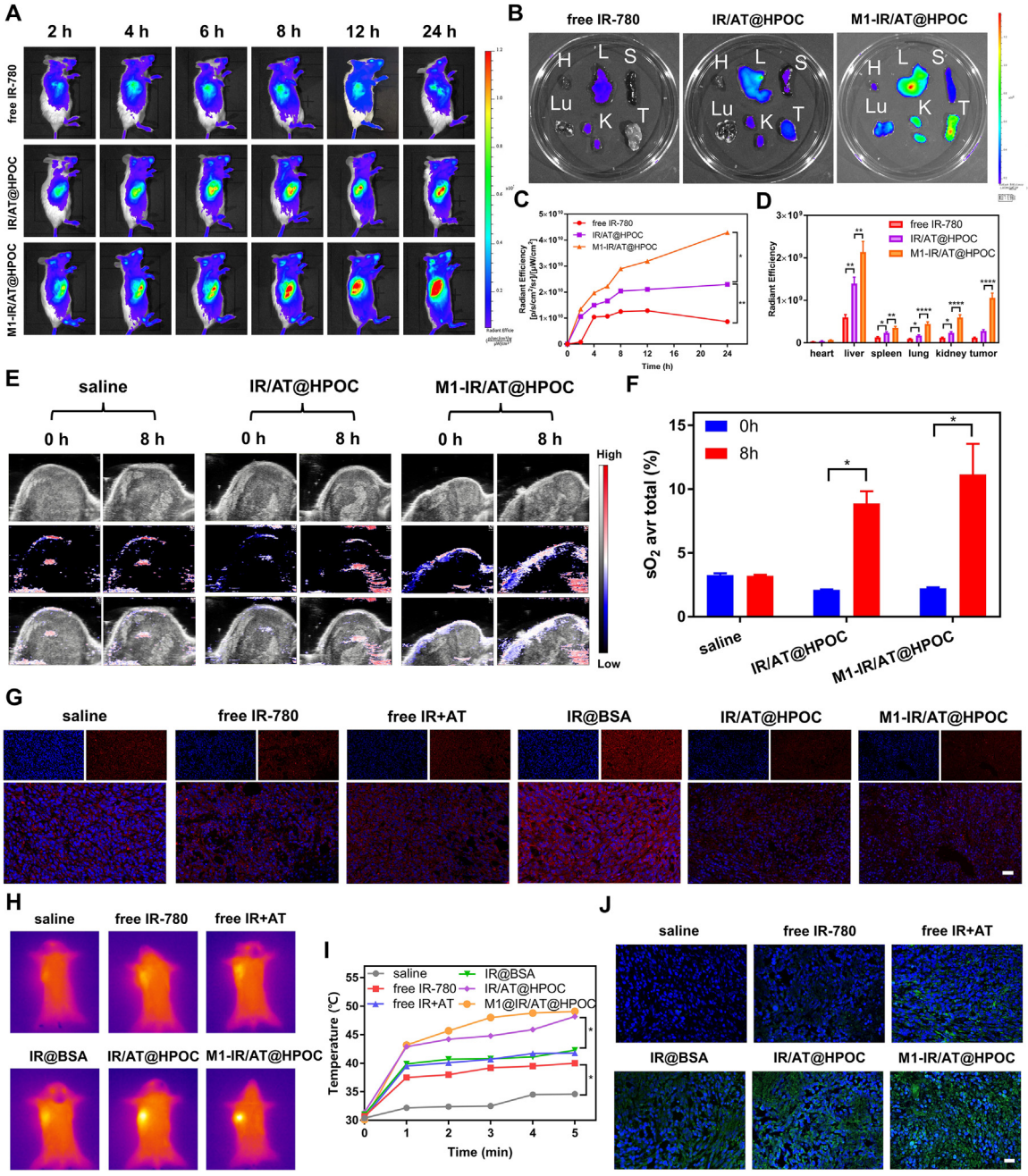

Fig. 5 – Tumor-targeted accumulation, oxygen delivery efficiency, PTT and PDT effect. (A) Representative fluorescence images of subcutaneous xenograft 4T1 tumor models after treatment with free IR-780, IR/AT@HPOC or M1-IR/AT@HPOC. (B) *Ex vivo* fluorescence images of main tissues excised from mice 24 h treated with free IR-780 IR/AT@HPOC or M1-IR/AT@HPOC (H: heart; L: liver; S: spleen; Lu: lung; K: kidney; T: tumor) and the total radiant efficiency ($n = 3$). (C) Quantitative statistics of fluorescence intensity of tumor-targeted accumulation. (D) Quantitative statistics of fluorescence intensity of main tissues. (E) Photoacoustic imaging and the change of signal intensity *in vivo* of mice post-injection of saline, IR/AT@HPOC or M1-IR/AT@HPOC ($n = 3$). (F) Quantitative statistics of signal intensity of HbO_2. (G) Confocal images of HIF-1α immunofluorescence staining in 4T1 tumor sections after various treatments exposed to NIR laser irradiation. Scale bar: 100 μm. (H) The thermal imaging of subcutaneous xenograft 4T1 tumor models in different groups exposed to NIR laser irradiation. (I) Temperature changes of 4T1 tumors in mice exposed to NIR laser irradiation. (J) Confocal images of ROS generation in 4T1 tumor sections after various treatments exposed to NIR laser irradiation. Scale bar: 50 μm.

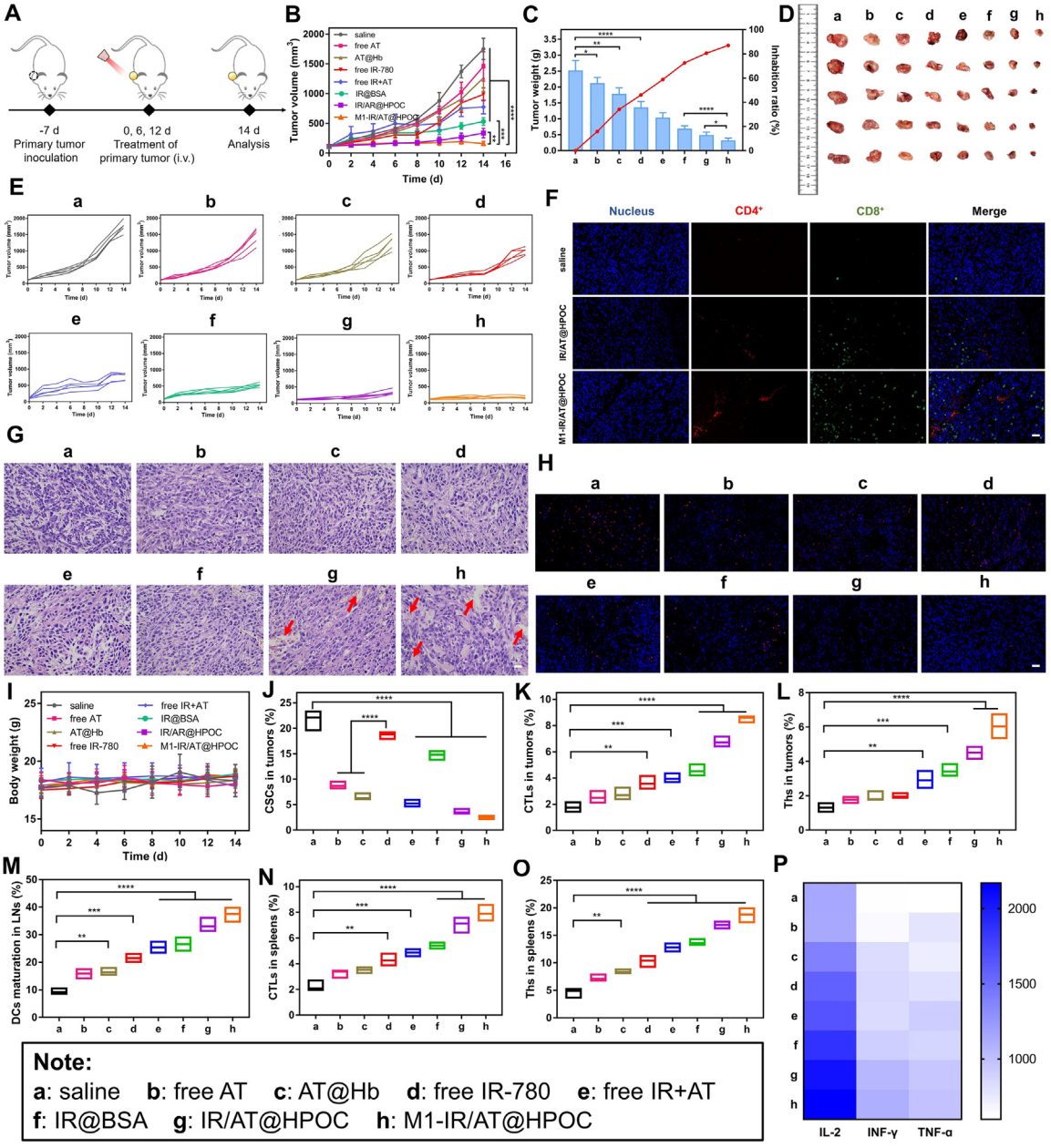

Fig. 6 – *In vivo* therapeutics and immunoregulation against 4T1 tumors. (A) Schematic illustration of intravenous injection of different formulations in subcutaneous xenograft 4T1 tumor models. (B) The tumor volume of mice treated with different preparations at indicated time ($n = 5$). (C) The tumor weight and tumor inhibition rates of mice treated with different formulations ($n = 5$). (D) Images of primary tumors in mice following different treatments. (E) The tumor volume of mice treated with the indiated preparations ($n = 5$). (F) Immunofluorescence staining images of $CD4^+$ T cells and $CD8^+$ T cells in 4T1 tumor sections after various treatments. Scale bar: 50 μm. (G) H&E assay of 4T1 tumor sections after various treatments. The area of tumor damage pointed by the arrow. Scale bar: 100 μm. (H) Confocal images of SOX2 immunofluorescence staining in 4T1 tumor sections after various treatments. Scale bar: 100 μm. (I) Body weight variations of mice receiving different treatments ($n = 5$). (J) Percentages of CSCs in tumors. (K) Percentages of CTLs in tumors. (L) Percentages of Ths in tumors. (M) Percentages of matured DCs in TDLNs. (N) Percentages of CTLs in spleens. (O) Percentages of Ths in spleens. (P) The concentrations of systemic cytokine (IL-2, IFN-γ and TNF-α) of mice treated with the indicated preparations ($n = 5$).

the results of tumor weight and tumor inhibition ratio, M1-IR/AT@HPOC presented the most efficient tumor suppression compared to other treatments (Fig. 6C). Positive staining of the TUNEL, known as a marker of apoptosis, indicated the most apoptosis bodies in M1-IR/AT@HPOC group, verifying that M1-IR/AT@HPOC could strongly induce the tumor cell apoptosis (Fig. S21). H&E analysis of the tumors from mice indicated that M1-IR/AT@HPOC resulted in extensive tumor cell death (Fig. 6G). No observable histological damage observed by the histological examination of major organs suggest that there was no obvious systemic toxicity after treatment (Fig. S22). Consistently, no obvious weight loss was found in the mice within the treatment, indicating the excellent biocompatibility of nanoplatform (Fig. 6I). By analyzing the kidney function indices including creatinine (CR) and blood urea nitrogen (BUN) and liver function indices including alanine transaminase (ALT) and aspartate transaminase (AST) in the blood of mice, there was no significant difference in the blood indexes of the treatment group compared with saline group and the blood chemistry analysis of each treatment group was within the safe range (Fig. S23).

The satisfactory antitumor efficacy of M1-IR/AT@HPOC might be attributed to the photothermal and photodynamic properties of IR-780, the differentiation-induction of ATRA, and the activation of antitumor immune response [58]. To reveal the inhibitory effect of the nanoplatform on CSCs *in vivo*, the $CD24^{-}CD44^{+}$ subpopulations in tumor tissues were analyzed by flow cytometry. In free AT or AT@Hb groups, the populations of CSCs in tumor tissues were 8.68% and 6.25%, respectively, which were significantly lower than those in saline group (22.1%), suggesting that ATRA could reduce the proportion of CSCs through the differentiation-inducing effect. With the combination of differentiation-inducing effects and phototherapy, IR/AT@HPOC significantly promoted the elimination of CSCs, evidently reducing the CSC population from 22.1% to 3.46%. More importantly, CSCs were significantly reduced in the M1-IR/AT@HPOC-treated group, and the lowest expression of $CD24^{-}CD44^{+}$ subsets was observed, suggesting that the targeting of M1-type macrophage membranes could increase the uptake of nanoparticles by tumor tissues (Fig. 6J and S25A). These experimental results revealed that the nanoplatform integrating phototherapy and differentiation induction of CSCs exhibited potent inhibitory effect on CSCs. In addition to flow cytometry analysis, the expression of CSCs markers including Nanog and SOX2 was evaluated by immunofluorescence staining. As illustrated in Fig. S24 and 6H, more positive cells for Nanog and SOX2 were observed in the saline group compared to the treatment group. Instead, a less fluorescent signal could be found in the slice after M1-IR/AT@HPOC treatment, implying that CSCs could be selectively inhibited by using the prepared nano-assemblies. Overall, combining differentiation-inducing effect with phototherapy, the proposed M1-IR/AT@HPOC could transform CSCs into non-CSCs and effectively eliminate CSCs.

To elucidate the underlying mechanism of desirable antitumor effect, the immunomodulatory effects *in vivo* were explored at the end of the antitumor study. DC activation in the TDLNs was assessed using flow cytometric measurement after the treatment. Combination therapy by M1-IR/AT@HPOC facilitated 37.5% of DC maturation, which was 4.07-fold more efficient than saline group, implying ICD induction of M1-IR/AT@HPOC significantly enhanced the tumor immunogenicity and promoted DC maturation in the TDLNs (Fig. 6M and S25D). Subsequently, the infiltration of CTLs and Ths in primary tumors at the end of treatment was analyzed through flow cytometry. M1-IR/AT@HPOC group resulted in the most pronounced CTLs infiltration (8.59%) and Ths infiltration (6.03%), which was 4.9 and 4.6 times higher than those of saline group, respectively (Fig. 6K-6L and S25B-S25C). In accordance with the immunofluorescent staining, the red and green fluorescence in sections of M1-IR/AT@HPOC group were clearly observed, showing that M1-IR/AT@HPOC enabled the most effective infiltration of $CD4^{+}$ and $CD8^{+}$ cells compared with saline group (Fig. 6F).

To further demonstrate the boosted systemic immunity of M1-IR/AT@HPOC, the distribution of CTLs and Ths in the spleen was detected by flow cytometric analysis after treatment. After the therapeutic period, M1-IR/AT@HPOC-mediated immunotherapy elicited 7.89% CTLs and 18.8% Ths in spleens, which was obviously higher than those of saline group (2.27% and 4.89%, respectively) (Fig. 6N-6O and S25E-S25F). Apart from immune cells, the production of key cytokines including IL-2, TNF-α and IFN-γ, which were typical biomarkers of cellular immune responses and sensitized tumors to cancer immunotherapy, was analyzed by ELISA. These data collectively suggested that the M1-IR/AT@HPOC group showed a significant increased level of IL-2, TNF-α and IFN-γ in serum, which was 2.0-fold (IL-2), 1.58-fold (TNF-α) and 1.69-fold (IFN-γ) higher than that of the saline group. The treatment of M1-IR/AT@HPOC boosted the production of these cytokines, which also strengthened the activity of effector T cells or attacked tumor cells directly to assist in suppressing tumor growth (Fig. 6P). In summary, the results convincingly reflected that M1-IR/AT@HPOC could enhance tumor regression and provoke a desirable systemic immune activation effect.

3.15. *In vivo anti-distant tumor therapy*

The ideal tumor treatment should not only focus on the removal of primary tumors, but also attach importance to the suppression of any distant tumor tissues. Given the capacity of M1-IR/AT@HPOC to elicit systemic immunity, the distal effects were validated in a bilateral 4T1 tumor-bearing mice (Fig. 7A). Laser treatments were performed only on the primary tumors, so the tumor-killing effect of IR-780 *via* PTT/PDT could not act on distant tumors. That is to say, the CSC clearance and tumor volume reduction in distal tumors were mainly caused by the differentiation induction effect and systemic anti-tumor immune response. We found that the treatment group with free ATRA or AT@Hb slightly postponed the growth of distant tumors compared to the saline group, mainly by activating a systemic immune response against distant tumors. The laser treatment group elicited a potent therapeutic efficacy against the progression of distant tumors relative to the non-laser treatment group. Notably, M1-IR/AT@HPOC group significantly suppressed the primary and distant tumor growth with the inhibition rate of 82.8% (Fig. 7B

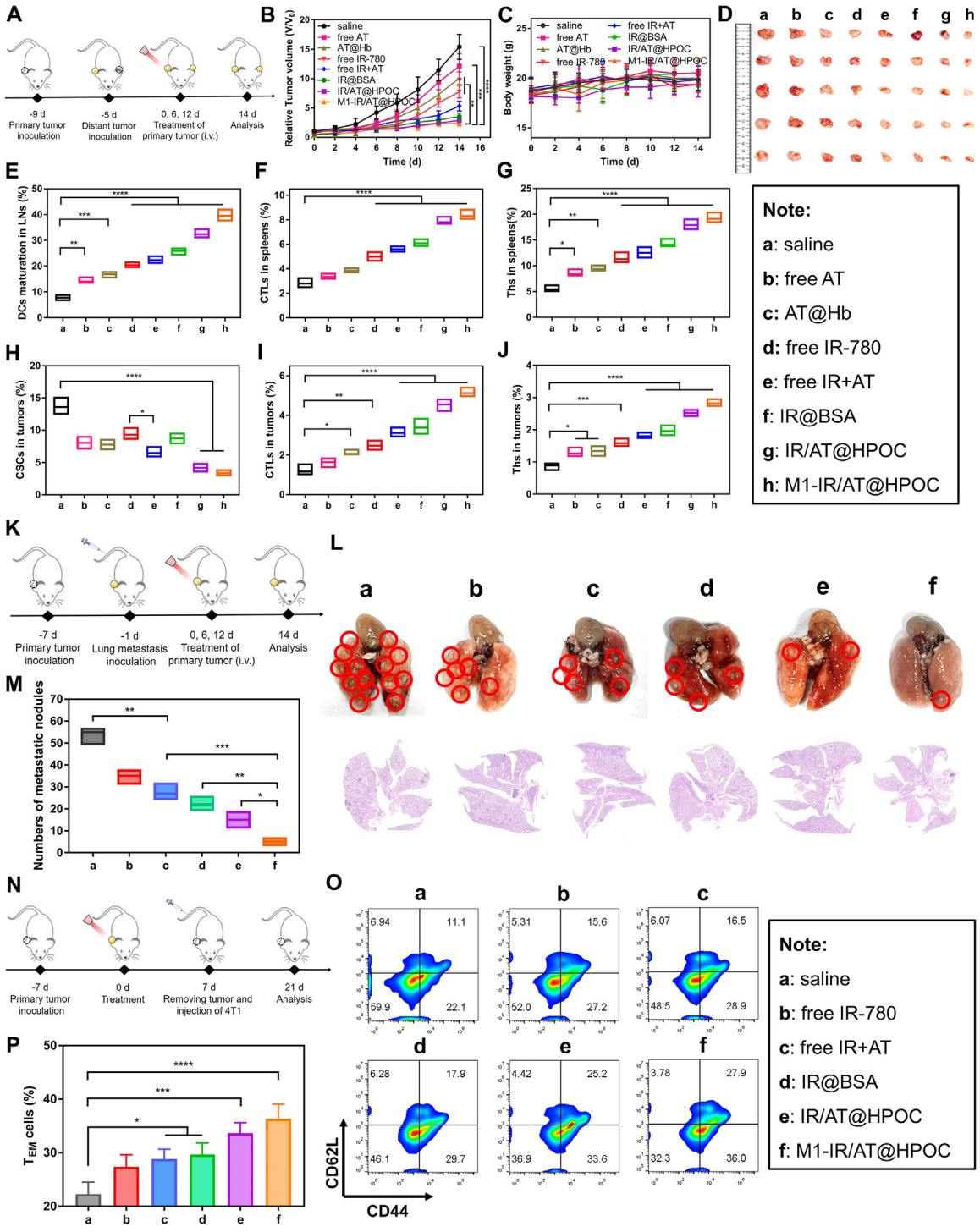

Fig. 7 – *In vivo* anti-distant tumor therapy, anti-metastasis activity and immune memory. (A) Schematic illustration of intravenous injection of different formulations in distant tumor models. (B) The distant tumor volume of mice treated with different preparations at indicated time ($n = 5$). (C) Body weight variations of mice receiving different treatments ($n = 5$). (D) Images of distant tumors in mice following different treatments. (E) Percentages of matured DCs in TDLNs. (F) Percentages of CTLs in spleens. (G) Percentages of Ths in spleens. (H) Percentages of CSCs in distant tumors. (I) Percentages of CTLs in distant tumors. (J) Percentages of Ths in distant tumors. (K)Schematic illustration of the 4T1 lung metastasis model. (L) Optical photographs and H&E staining of lungs in mice after different treatments. (M) Numbers of pulmonary nodules in different treatment groups ($n = 3$). (N) Schematic illustration of long-term immune response. (O) Flow analysis of the proportion of T_{EM} in spleens of mice after different treatments. (P) The percentages of the T_{EM} in spleens receiving different treatments ($n = 3$).

and 7D) and 84.38% (Fig. S26), respectively. According to the body weight curve of mice, the mice body weight did not decrease significantly after different treatments (Fig. 7C). Besides, the H&E images of distant tumors exhibited that M1-IR/AT@HPOC group was superior to other treatment groups in inhibiting distant tumors (Fig. S27).

Encouraged by the prominent inhibitory abilities of distant tumors, immune phenotyping was performed on the TDLNs, spleens, and tumors in different groups. The DC activation in TDLNs was first analyzed by flow cytometry. Consistent with the results of DC maturation in the primary tumor, the percentage of DC maturation in the M1-IR/AT@HPOC group (39.5%) was clearly higher than in all other treatment groups (Fig. 7E and S28A). Sequentially, the individual populations of CTLs and Ths were further identified in spleens. M1-IR/AT@HPOC group produced the most excessive CTLs and Ths compared to other groups, proving the successful activation of systemic anti-tumor immunity (Fig. 7F-7G and S28B-S28C). Separately, the CSC population in the M1-IR/AT@HPOC group were much lower than other treatment groups (Fig. 7H and S28D). These results were further corroborated by the populations of CTLs and Ths infiltrated in distant tumors (5.12% and 2.82%), which were 4.38 and 3.17 times higher than in saline group (1.17% and 0.89%), respectively. The population rate of CTLs and Ths was increased in response to the synergistic effect of phototherapy and differentiation therapy, which accounted for the distant tumor growth inhibition (Fig. 7I-7J and S28E-S28F). Collectively, all these results indicated that M1-IR/AT@HPOC triggered the systemic anti-tumor immune response and differentiation induction effect in distant tumors as well as provided non-local treatment for distant and metastatic tumors that cannot be reached by laser irradiation.

3.16. *In vivo anti-metastasis effect*

Since M1-IR/AT@HPOC treatment was proved to significantly inhibit tumor growth and successfully provoke immune response, a lung metastasis model was constructed to evaluate its anti-tumor metastasis performance according to the procedures as described in Fig. 7K. The mice that were pretreated with the M1-IR/AT@HPOC exhibited fewer lung metastatic nodules, while the saline group was found to bear massive pulmonary nodules after 14 d (Fig. 7L). The statistics of pulmonary nodule numbers was further confirmed the anti-tumor metastasis efficacy of M1-IR/AT@HPOC treatment as indicated in Fig. 7M. Numerous metastatic nodules were observed in saline group (54 ± 4). Remarkably, M1-IR/AT@HPOC group prominently reduced the number of pulmonary nodules (5 ± 2). The H&E staining images also exhibited the above results, proving the availability of combined phototherapy and differentiation therapy in suppressing tumor metastasis.

3.17. *In vivo immune memory*

As a significant feature of adaptive immunity, immune memory can prevent the recurrence of tumor for a long time. Memory T cells are critical for long-term tumor regression [59]. The long-term immune memory response was analyzed after various treatments to probe the underlying mechanism of long-term inhibition of tumor recurrence (Fig. 7N). From Fig. 7O, it could be observed that the frequency of T_{EM} in the spleen for mice treated with M1-IR/AT@HPOC dramatically increased from 22.1% to 36% in comparison with the saline group (Fig. 7P) [60]. These experimental results implied that M1-IR/AT@HPOC effectively activated memory immune effect through phototherapy, ICD induction and differentiation induction effect [42].

4. Conclusion

In summary, we constructed a versatile pH-sensitive nanoplatform through the biomineralization method for achieving synergistic treatment of phototherapy and differentiation therapy. We demonstrated that prepared nanoclusters enabled to be decomposed into individual small-diameter AT@Hb and IR@BSA complexes in an acidic environment for significantly improving the intratumoral penetration. The released AT@Hb could not only differentiate CSCs into non-CSCs, but also relieve tumor hypoxia through the oxygen carried by Hb, thereby converting CSC niche to a hostile condition for CSCs survival for synergetic eradication of CSCs. Simultaneously, the released IR@BSA under light irradiation would generate hyperthermia and ROS for eliminating CSCs and bulk tumor cells. Importantly, the destruction of tumor cells induced by IR-780 could be further amplified by the differentiation effect of ATRA, and then elicit large-scale ICD phenomenon. Such nanosystem could suppress primary and distant tumor growth and their pulmonary metastasis through multiple therapeutic pathways, which simultaneously offered tumor-specific immune memory to protect mice from cancer rechallenge. Consequently, this work provides a new light on the synergistic effect of differentiation therapy and phototherapy and bridges cancer stem cell inhibition and immunotherapy, laying a theoretical foundation for a new combination model of cancer therapy.

Conflicts of interest

There are no conflicts to declare.

Acknowledgements

This work is supported by National Science and Technology Major Special Project-Major New Drug Creation (2019ZX09301-112) and Shandong Natural Science Foundation (ZR2020QH351), Shandong Provincial Program of Taishan Industrial Experts (2019TSCYCX-31) and the Fundamental Research Funds of Shandong University (2020GN091).

Supplementary materials

Supplementary material associated with this article can be found, in the online version, at doi:10.1016/j.ajps.2023.100851.

References

[1] Li H, Yan W, Suo X, Peng H, Yang X, Li Z, et al. Nucleus-targeted nano delivery system eradicates cancer stem cells by combined thermotherapy and hypoxia-activated chemotherapy. Biomaterials 2019;200:1–14.

[2] Guan J, Wu Y, Liu X, Wang H, Ye N, Li Z, et al. A novel prodrug and its nanoformulation suppress cancer stem cells by inducing immunogenic cell death and inhibiting indoleamine 2, 3-dioxygenase. Biomaterials 2021;279:121180.

[3] Pan Y, Zhou S, Li Y, Parshad B, Li W, Haag R. Novel dendritic polyglycerol-conjugated, mesoporous silica-based targeting nanocarriers for co-delivery of doxorubicin and tariquidar to overcome multidrug resistance in breast cancer stem cells. J Control Release 2021;330:1106–17.

[4] Wang F, Luo R, Xin H, Zhang Y, Córdova Wong BJ, Wang W, et al. Hypoxia-stimulated tumor therapy associated with the inhibition of cancer cell stemness. Biomaterials 2020;263:120330.

[5] Mauri F, Schepkens C, Lapouge G, Drogat B, Song Y, Pastushenko I, et al. NR2F2 controls malignant squamous cell carcinoma state by promoting stemness and invasion and repressing differentiation. Nat Cancer 2021;2(11):1152–69.

[6] Shen S, Xu X, Lin S, Zhang Y, Liu H, Zhang C, et al. A nanotherapeutic strategy to overcome chemotherapeutic resistance of cancer stem-like cells. Nat Nanotechnol 2021;16(1):104–13.

[7] Huang H, Shi H, Liu J, Min Y, Wang Y, Wang AZ, et al. Co-delivery of all-trans-retinoic acid enhances the anti-metastasis effect of albumin-bound paclitaxel nanoparticles. Chem Comm 2017;53(1):212–15.

[8] Lu F, Li Z, Sheng Y, Ma Y, Yang Y, Ren Y, et al. Thermal-triggered packing of lipophilic NIR dye IR780 in hepatitis B core at critical ionic strength and cargo-host ratio for improved stability and enhanced cancer phototherapy. Biomaterials 2021;276:121035.

[9] Luo S, Wang Y, Shen S, Tang P, Liu Z, Zhang S, et al. IR780-loaded hyaluronic acid@gossypol–Fe(III)–EGCG infinite coordination polymer nanoparticles for highly efficient tumor photothermal/coordinated dual drugs synergistic therapy. Adv Funct Mater 2021;31(24):2100954.

[10] Mo Z, Qiu M, Zhao K, Hu H, Xu Q, Cao J, et al. Multifunctional phototheranostic nanoplatform based on polydopamine-manganese dioxide-IR780 iodide for effective magnetic resonance imaging-guided synergistic photodynamic/photothermal therapy. J Colloid Interf Sci 2022;611:193–204.

[11] Lopez-Bertoni H, Kozielski KL, Rui Y, Lal B, Vaughan H, Wilson DR, et al. Bioreducible polymeric nanoparticles containing multiplexed cancer stem cell regulating miRNAs inhibit glioblastoma growth and prolong survival. Nano Lett 2018;18(7):4086–94.

[12] Chen P, Hsu WH, Han J, Xia Y, DePinho RA. Cancer stemness meets immunity: from mechanism to therapy. Cell Rep 2021;34(1):108597.

[13] Wang C, Wang Q, Wang H, Li Z, Chen J, Zhang Z, et al. Hydroxyethyl starch-folic acid conjugates stabilized theranostic nanoparticles for cancer therapy. J Control Release 2023;353:391–410.

[14] Tan T, Wang H, Cao H, Zeng L, Wang Y, Wang Z, et al. Deep tumor-penetrated nanocages improve accessibility to cancer stem cells for photothermal-chemotherapy of breast cancer metastasis. Adv Sci 2018;5(12):1801012.

[15] Pan Y, Ma X, Liu C, Xing J, Zhou S, Parshad B, et al. Retinoic acid-loaded dendritic polyglycerol-conjugated gold nanostars for targeted photothermal therapy in breast cancer stem cells. ACS Nano 2021;15(9):15069–84.

[16] Yu LY, Shueng PW, Chiu HC, Yen YW, Kuo TY, Li CR, et al. Glucose transporter 1-mediated transcytosis of glucosamine-labeled liposomal ceramide targets hypoxia niches and cancer stem cells to enhance therapeutic efficacy. ACS Nano 2023;17(14):13158–75.

[17] An J, Tang S, Hong G, Chen W, Chen M, Song J, et al. An unexpected strategy to alleviate hypoxia limitation of photodynamic therapy by biotinylation of photosensitizers. Nat Commun 2022;13(1):2225.

[18] Wang Y, Luo S, Wu Y, Tang P, Liu J, Liu Z, et al. Highly penetrable and on-demand oxygen release with tumor activity composite nanosystem for photothermal/photodynamic synergetic therapy. ACS Nano 2020;14(12):17046–62.

[19] Yuan M, Liang S, Zhou Y, Xiao X, Liu B, Yang C, et al. A robust oxygen-carrying hemoglobin-based natural sonosensitizer for sonodynamic cancer therapy. Nano Lett 2021;21(14):6042–50.

[20] Jia Y, Duan L, Li J. Hemoglobin-based nanoarchitectonic assemblies as oxygen carriers. Adv Mater 2016;28(6):1312–18.

[21] Yu Q, Qiu Y, Li J, Tang X, Wang X, Cun X, et al. Targeting cancer-associated fibroblasts by dual-responsive lipid-albumin nanoparticles to enhance drug perfusion for pancreatic tumor therapy. J Control Release 2020;321:564–75.

[22] Yang G, Phua SZF, Lim WQ, Zhang R, Feng L, Liu G, et al. A hypoxia-responsive albumin-based nanosystem for deep tumor penetration and excellent therapeutic efficacy. Adv Mater 2019;31(25):1901513.

[23] Yang Z, Chen Q, Chen J, Dong Z, Zhang R, Liu J, et al. Tumor-pH-responsive dissociable albumin–tamoxifen nanocomplexes enabling efficient tumor penetration and hypoxia relief for enhanced cancer photodynamic therapy. Small 2018;14(49):1803262.

[24] Chen Z, Liu L, Liang R, Luo Z, He H, Wu Z, et al. Bioinspired hybrid protein oxygen nanocarrier amplified photodynamic therapy for eliciting anti-tumor immunity and abscopal effect. ACS Nano 2018;12(8):8633–45.

[25] Jiang Z, Liu Y, Shi R, Feng X, Xu W, Zhuang X, et al. Versatile polymer-initiating biomineralization for tumor blockade therapy. Adv Mater 2022;34(19):2110094.

[26] Zhang S, Zhang Y, Feng Y, Wu J, Hu Y, Lin L, et al. Biomineralized two-enzyme nanoparticles regulate tumor glycometabolism inducing tumor cell pyroptosis and robust antitumor immunotherapy. Adv Mater 2022;34(50):2206851.

[27] Jana D, He B, Chen Y, Liu J, Zhao Y. A defect-engineered nanozyme for targeted NIR-II photothermal immunotherapy of cancer. Adv Mater 2022;n/a(n/a):2206401.

[28] Zhen W, Liu Y, Lin L, Bai J, Jia X, Tian H, et al. BSA-IrO_2: catalase-like nanoparticles with high photothermal conversion efficiency and a high X-ray absorption coefficient for anti-inflammation and antitumor theranostics. Angew Chem Int Ed 2018;57(32):10309–13.

[29] Zhu Y, Xue J, Chen W, Bai S, Zheng T, He C, et al. Albumin-biomineralized nanoparticles to synergize phototherapy and immunotherapy against melanoma. J Control Release 2020;322:300–11.

[30] Hu C, Lei T, Wang Y, Cao J, Yang X, Qin L, et al. Phagocyte-membrane-coated and laser-responsive nanoparticles control primary and metastatic cancer by inducing anti-tumor immunity. Biomaterials 2020;255:120159.

[31] Xuan M, Shao J, Dai L, He Q, Li J. Macrophage cell membrane camouflaged mesoporous silica nanocapsules for *in vivo* cancer therapy. Adv Healthc Mater 2015;4(11):1645–52.

[32] Chen Q, Feng L, Liu J, Zhu W, Dong Z, Wu Y, et al. Intelligent albumin-MnO_2 nanoparticles as pH-/H_2O_2-responsive dissociable nanocarriers to modulate tumor hypoxia for effective combination therapy. Adv Mater 2018;30(8):1707414.

[33] Xu T, Ma Y, Yuan Q, Hu H, Hu X, Qian Z, et al. Enhanced ferroptosis by oxygen-boosted phototherapy based on a 2-in-1 nanoplatform of ferrous hemoglobin for tumor synergistic therapy. ACS Nano 2020;14(3):3414–25.
[34] Sheng Z, Hu D, Zheng M, Zhao P, Liu H, Gao D, et al. Smart human serum albumin-indocyanine green nanoparticles generated by programmed assembly for dual-modal imaging-guided cancer synergistic phototherapy. ACS Nano 2014;8(12):12310–22.
[35] Yu Q, Tang X, Zhao W, Qiu Y, He J, Wan D, et al. Mild hyperthermia promotes immune checkpoint blockade-based immunotherapy against metastatic pancreatic cancer using size-adjustable nanoparticles. Acta Biomater 2021;133:244–56.
[36] Chen Q, Liu X, Chen J, Zeng J, Cheng Z, Liu Z. A self-assembled albumin-based nanoprobe for *in vivo* ratiometric photoacoustic pH imaging. Adv Mater 2015;27(43):6820–7.
[37] Hirschmann-Jax C, Foster AE, Wulf GG, Nuchtern JG, Jax TW, Gobel U, et al. A distinct "side population" of cells with high drug efflux capacity in human tumor cells. Proc Natl Acad Sci 2004;101(39):14228–33.
[38] Lang T, Liu Y, Zheng Z, Ran W, Zhai Y, Yin Q, et al. Cocktail strategy based on spatio-temporally controlled nano device improves therapy of breast cancer. Adv Mater 2019;31(5):1806202.
[39] Shao X, Ding Z, Zhou W, Li Y, Li Z, Cui H, et al. Intrinsic bioactivity of black phosphorus nanomaterials on mitotic centrosome destabilization through suppression of PLK1 kinase. Nat Nanotechnol 2021;16(10):1150–60.
[40] Li Q, Zhao Z, Qin X, Zhang M, Du Q, Li Z, et al. A checkpoint-regulatable immune niche created by injectable hydrogel for tumor therapy. Adv Funct Mater 2021;31(37):2104630.
[41] Feng B, Hou B, Xu Z, Saeed M, Yu H, Li Y. Self-amplified drug delivery with light-inducible nanocargoes to enhance cancer immunotherapy. Adv Mater 2019;31(40):1902960.
[42] Tang H, Xu X, Chen Y, Xin H, Wan T, Li B, et al. Reprogramming the tumor microenvironment through second-near-infrared-window photothermal genome editing of PD-L1 mediated by supramolecular gold nanorods for enhanced cancer immunotherapy. Adv Mater 2021;33(12):2006003.
[43] Cao H, Dan Z, He X, Zhang Z, Yu H, Yin Q, et al. Liposomes coated with isolated macrophage membrane can target lung metastasis of breast cancer. ACS Nano 2016;10(8):7738–48.
[44] Wang Y, Zhang K, Li T, Maruf A, Qin X, Luo L, et al. Macrophage membrane functionalized biomimetic nanoparticles for targeted anti-atherosclerosis applications. Theranostics 2021;11(1):164–80.
[45] Gao S, Liu Y, Liu M, Yang D, Zhang M, Shi K. Biodegradable mesoporous nanocomposites with dual-targeting function for enhanced anti-tumor therapy. J Control Release 2022;341:383–98.
[46] Shi J, Yu W, Xu L, Yin N, Liu W, Zhang K, et al. Bioinspired nanosponge for salvaging ischemic stroke *via* free radical scavenging and self-adapted oxygen regulating. Nano Lett 2020;20(1):780–9.
[47] Li X, Liu L, Li S, Wan Y, Chen JX, Tian S, et al. Biodegradable π-conjugated oligomer nanoparticles with high photothermal conversion efficiency for cancer theranostics. ACS Nano 2019;13(11):12901–11.
[48] Feng Z, Yu X, Jiang M, Zhu L, Zhang Y, Yang W, et al. Excretable IR-820 for *in vivo* NIR-II fluorescence cerebrovascular imaging and photothermal therapy of subcutaneous tumor. Theranostics 2019;9(19):5706–19.
[49] Liu R, An Y, Jia W, Wang Y, Wu Y, Zhen Y, et al. Macrophage-mimic shape changeable nanomedicine retained in tumor for multimodal therapy of breast cancer. J Control Release 2020;321:589–601.
[50] Zhu X, Li L, Tang J, Yang C, Yu H, Liu K, et al. Cascade-responsive nano-assembly for efficient photothermal-chemo synergistic inhibition of tumor metastasis by targeting cancer stem cells. Biomaterials 2022;280:121305.
[51] Li Y, Lin J, Wang P, Luo Q, Zhu F, Zhang Y, et al. Tumor microenvironment cascade-responsive nanodrug with self-targeting activation and ROS regeneration for synergistic oxidation-chemotherapy. Nano-Micro Lett 2020;12(1):182.
[52] Zhao T, Liang C, Zhao Y, Xue X, Ma Z, Qi J, et al. Multistage pH-responsive codelivery liposomal platform for synergistic cancer therapy. J Nanobiotechnol 2022;20(1):177.
[53] Liu XL, Dong X, Yang SC, Lai X, Liu HJ, Gao Y, et al. Biomimetic liposomal nanoplatinum for targeted cancer chemophototherapy. Adv Sci 2021;8(8):2003679.
[54] Li Z, Xu W, Yang J, Wang J, Wang J, Zhu G, et al. A tumor microenvironments-adapted polypeptide hydrogel/nanogel composite boosts antitumor molecularly targeted inhibition and immunoactivation. Adv Mater 2022;34(21):2200449.
[55] Xu Y, Guo Y, Zhang C, Zhan M, Jia L, Song S, et al. Fibronectin-coated metal–phenolic networks for cooperative tumor chemo-/chemodynamic/immune therapy *via* enhanced ferroptosis-mediated immunogenic cell death. ACS Nano 2022;16(1):984–96.
[56] Zhang S, Wang J, Kong Z, Sun X, He Z, Sun B, et al. Emerging photodynamic nanotherapeutics for inducing immunogenic cell death and potentiating cancer immunotherapy. Biomaterials 2022;282:121433.
[57] Chen J, Liang C, Song X, Yi X, Yang K, Feng L, et al. Hybrid protein nano-reactors enable simultaneous increments of tumor oxygenation and iodine-131 delivery for enhanced radionuclide therapy. Small 2019;15(46):1903628.
[58] Huang J, Zhang L, Zhou W, Wang J, Zhang R, Wang Z, et al. Dual mitigation of immunosuppression combined with photothermal inhibition for highly effective primary tumor and metastases therapy. Biomaterials 2021;274:120856.
[59] Wu W, Pu Y, Gao S, Shen Y, Zhou M, Yao H, et al. Bacterial metabolism-initiated nanocatalytic tumor immunotherapy. Nano-Micro Lett 2022;14(1):220.
[60] Liu J, He S, Luo Y, Zhang Y, Du X, Xu C, et al. Tumor-microenvironment-activatable polymer nano-immunomodulator for precision cancer photoimmunotherapy. Adv Mater 2022;34(8):2106654.